On viscous film flows coating the interior of a tube: thin-film and long-wave models

Roberto Camassa[1] and H. Reed Ogrosky[2],†

[1]Carolina Center for Interdisciplinary Applied Mathematics, Department of Mathematics,
University of North Carolina, Chapel Hill, NC 27599-3250, USA

[2]Department of Mathematics, University of Wisconsin, Madison, WI 53706-1325, USA

A theoretical and numerical investigation of two classes of models for pressure-driven core–annular flow is presented. Both classes, referred to as 'long-wave' and 'thin-film' models, may be derived from a unified perspective using long-wave asymptotics, but are distinct from one another in the role played by the curved tube geometry with respect to the planar (limiting) case. Analytical and numerical techniques are used to show and quantify the significant differences between the behaviour of solutions to both model types. Temporal linear stability analysis of the constant solution is carried out first to pinpoint with closed-form mathematical expressions the different dynamical regimes associated with absolute or convective instabilities. Numerical simulations for the models are then performed and qualitative differences in the evolution of the free surface are explored. Mathematically, different levels of asymptotic accuracy are found to result in different regularizing properties affecting the long-time behaviour of generic numerical solutions. Travelling wave solutions are also studied, and qualitative differences in the topology of streamline patterns describing the flow of the film in a moving reference frame are discussed. These topological differences allow for further classification of the models. In particular, a transition from a regime in which waves trap a fluid core to one where waves travel faster than any parcel of the underlying fluid is documented for a variant of the primary model. In the corresponding thin-film model, no such transition is found to occur. The source of these differences is examined, and a comparison of the results with those of related models in the literature is given. A brief discussion of the merits of each class of models concludes this study.

Key words: core–annular flow, instability, thin films

1. Introduction

Viscous liquid film flows have received much attention over recent decades due to their presence in numerous industrial and biological applications. Such flows have a free surface, often an interface between air and liquid, which can be unstable to long-wave perturbations, as demonstrated by, e.g., Goren (1962), Yih (1967) and Hickox (1971). A desire to better understand these flows and their instabilities has driven

† Email address for correspondence: ogrosky@math.wisc.edu

the development of many asymptotic models that encapsulate the fundamental physics of the free surface evolution without the complexity of the parent equations. One such approach assumes that the amplitude of perturbations of an exact (flat interface) solution is small relative to the thickness of the film. The resulting weakly nonlinear models have given insight into the cause and nature of instability development; see, e.g., Papageorgiou, Maldarelli & Rumschitzki (1990) and Joseph & Renardy (1993). In many flows of practical interest, however, instabilities saturate well outside of the weakly nonlinear regime, exposing the limitation of the weak nonlinearity assumption and giving rise to the need to develop models capable of handling large-amplitude dynamics.

Strongly nonlinear models for flows over either a flat or a curved surface have typically been derived by exploiting a small ratio of length scales, often the film thickness to a typical wavelength. These 'long-wave' asymptotic models have been used successfully to describe many flows, see, e.g., the review articles by Oron, Davis & Bankoff (1997) and Craster & Matar (2009). Viscous film flows over a curved surface offer a second natural choice of length scale ratio, namely the film thickness versus a radial scale (such as, e.g., a tube or fibre radius); here, we will refer to models derived under the assumption that the film thickness is small with respect to a radial scale as 'thin-film', and note that these models can be derived directly from the governing equations or recovered from their long-wave counterparts in the appropriate limit. While both the terms 'thin-film' and 'long-wave' are often used interchangeably in the literature to describe asymptotic models derived for film flows over flat surfaces, the distinction becomes somewhat necessary for flows over curved surfaces, which are the subject of the present study.

In axisymmetric flows along cylindrical surfaces, both modelling approaches of long-wave and thin-film result in a single nonlinear partial differential equation (PDE) for the evolution of the film's free surface. However, thin-film models have been somewhat more popular as (i) the nonlinearities that arise are generally of a much simpler form than their long-wave model counterparts, (ii) elimination of the thin-film parameter from the evolution equation reduces the dimensions of the parameter space by one and (iii) they bear a strong resemblance in form to well-studied models for corresponding film flows over flat surfaces. This resemblance to flat-surface models reflects the way in which taking the thin-film limit can 'flatten' the geometry by making the local curvature of the surface negligible over the scale of the film thickness, thus simplifying the cylindrical geometry effects retained in long-wave models.

We will consider here the specific problem of the axisymmetric flow of a viscous film which coats the interior of a cylinder, and focus on the case where the core region consisting of a second fluid (air or liquid) is forced to flow due to an imposed pressure gradient. Long-wave models for this core–annular flow problem in the case where the ratio of annular-to-core fluid viscosities is large were derived in Camassa & Lee (2006) and Camassa *et al.* (2012), with the latter incorporating the effects of different core and annular fluid densities. Corresponding thin-film models can be recovered in the appropriate limit; for the case of equal density fluids, a model in this limit was derived directly from the governing equations by Kerchman (1995).

The primary purpose of this paper is to demonstrate both qualitative and quantitative differences between the behaviour of solutions to these two classes of models for viscous-dominated core–annular flow. This is done through a detailed quantitative assessment of solutions to both classes of models using analytical and numerical tools. This assessment reveals qualitative differences in (i) the transient growth of

free surface instabilities in both the linear and nonlinear regimes, (ii) the behaviour and structure of saturated free surface instabilities and (iii) the streamline topology within the annular fluid flow. New mathematical and physical arguments are given to demonstrate the manner in which important effects of the cylindrical geometry are lost when taking the thin-film limit.

This primary purpose is achieved by implementing a unifying and organizing viewpoint of the various classes of models that have appeared in the literature for related problems. This is done in two steps. First, a general long-wave model for fully coupled core–annular flow is derived and presented; the new model encompasses the equations in Camassa & Lee (2006) and Camassa *et al.* (2012) which can be recovered in the appropriate large-viscosity-ratio limit. Second, by taking additional appropriate limits, the model in Camassa *et al.* (2012) is shown to contain other long-wave and thin-film models which have been derived to study the free surface of an interior viscous liquid coating under the influence of some combination of gravity, pressure-driven core flow and capillary forces (Hammond 1983; Frenkel 1992; Kerchman 1995; Camassa, Ogrosky & Olander 2014). The resulting hierarchy of models is documented, and analogies with the case of an exterior liquid coating documented in Craster & Matar (2009) are made.

The rest of the paper is organized as follows. In § 2, long-wave equations for the fully coupled core–annular flow are derived, and both the long-wave models derived in Camassa & Lee (2006) and Camassa *et al.* (2012) as well as their thin-film counterpart models are recovered in the appropriate limit of large viscosity ratio. Linear stability analysis of these four model equations is performed in § 3. Numerical solutions to two of the model equations will be discussed in § 4. In addition, travelling wave solutions are found numerically, and the associated motion of fluid parcels is studied. A discussion of how these results compare with those of related models is given in § 5, and an extended hierarchy of models is documented. Conclusions are given in § 6. Some details of the derivation of the fully coupled long-wave equations are found in appendix A.

2. Long-wave asymptotic models

The problem to be studied is that of a highly viscous film which coats the interior of a vertical rigid tube with radius $\bar{a}$. Henceforth, all dimensional quantities are marked by overbars (except for those quantities that are obviously dimensional, e.g. density ρ, viscosity μ, surface tension γ, etc.). The core region of the tube is occupied by another, possibly less viscous, fluid which may be forced to flow upwards against gravity by an imposed pressure gradient, resulting in a constant volume flux $\bar{Q}^{(c)}$. The resulting total volume flux for both fluids is denoted by $\bar{Q} = \bar{Q}^{(c)} + \bar{Q}^{(a)}$, where $\bar{Q}^{(a)}$ is the volume flux of the annular fluid. The flow is assumed to be axisymmetric so that the independent coordinates are $(\bar{r}, \bar{z})$, with $\bar{z}$ taken to be positive moving up the tube. Here, $\bar{r} = 0$ and $\bar{r} = \bar{a}$ correspond to the centre and wall of the tube respectively. The location of the free surface is denoted by $\bar{R}(\bar{z}, \bar{t})$; see figure 1(*a*) for a definition sketch of the flow variables.

Using long-wave asymptotics, models have previously been derived for core–annular flows where the annular film has much higher viscosity than the core fluid; the case where both fluids have equal density was derived in Camassa & Lee (2006), while the case of unequal densities was treated in Camassa *et al.* (2012). We summarize these models next, and show how they derive in an appropriate limit from a 'master' long-wave model for fully coupled core–annular flows (i.e. no assumed large viscosity ratio). Corresponding thin-film models are subsequently recovered in the limit of small film thickness.
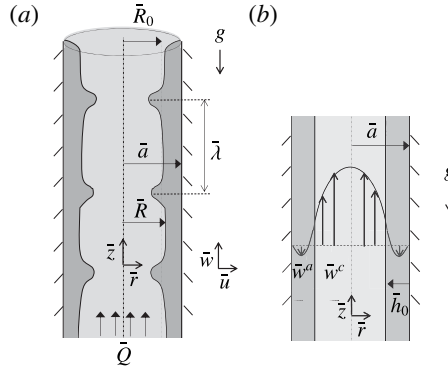
FIGURE 1. (*a*) Definition sketch of the flow variables. $\bar{R}$ denotes the location of the interface, $\bar{R}_0$ is the mean radius of the core region, $\bar{\lambda}$ is a typical free-surface wavelength, $(\bar{u}, \bar{w})$ are the velocity components in the $(\bar{r}, \bar{z})$ direction, and g is acceleration due to gravity. (*b*) Velocity profile of the flat-interface exact solution to the governing equations. $\bar{h}_0$ is the mean thickness of the annular film.

2.1. *Governing equations*

The governing equations for the flow of each fluid are the cylindrical axisymmetric Navier–Stokes equations,

$$\rho^i(\bar{u}^i_{\bar{t}} + \bar{u}^i\bar{u}^i_{\bar{r}} + \bar{w}^i\bar{u}^i_{\bar{z}}) = -\bar{p}^i_{\bar{r}} + \mu^i\left(\frac{1}{\bar{r}}\partial_{\bar{r}}(\bar{r}\bar{u}^i_{\bar{r}}) + \bar{u}^i_{\bar{z}\bar{z}} - \frac{\bar{u}^i}{\bar{r}^2}\right), \tag{2.1}$$

$$\rho^i(\bar{w}^i_{\bar{t}} + \bar{u}^i\bar{w}^i_{\bar{r}} + \bar{w}^i\bar{w}^i_{\bar{z}}) = -\bar{p}^i_{\bar{z}} + \mu^i\left(\frac{1}{\bar{r}}\partial_{\bar{r}}(\bar{r}\bar{w}^i_{\bar{r}}) + \bar{w}^i_{\bar{z}\bar{z}}\right) - \rho^i g, \tag{2.2}$$

$$\frac{1}{\bar{r}}\partial_{\bar{r}}(\bar{r}\bar{u}^i) + \bar{w}^i_{\bar{z}} = 0, \tag{2.3}$$

where $i = (a)$ corresponds to the annular film and $i = (c)$ to the core fluid. Here, $(\bar{u}, \bar{w})$ are the velocity components in the $(\bar{r}, \bar{z})$ directions respectively, $\bar{p}$ is pressure, ρ is density, μ is molecular viscosity and g is gravity. Subscripts denote partial derivatives. The boundary conditions at the wall, $\bar{r} = \bar{a}$, are no-slip,

$$\bar{u}^{(a)} = 0, \quad \bar{w}^{(a)} = 0, \tag{2.4a,b}$$

while at the free surface, $\bar{r} = \bar{R}(\bar{z}, \bar{t})$, the boundary conditions

$$\bar{u}^{(a)} = \bar{u}^{(c)}, \quad \bar{w}^{(a)} = \bar{w}^{(c)}, \tag{2.5a,b}$$

$$\mu^{(a)}[(\bar{w}^{(a)}_{\bar{r}} + \bar{u}^{(a)}_{\bar{z}})(1 - \bar{R}^2_{\bar{z}}) + 2(\bar{u}^{(a)}_{\bar{r}} - \bar{w}^{(a)}_{\bar{z}})\bar{R}_{\bar{z}}]$$
$$= \mu^{(c)}[(\bar{w}^{(c)}_{\bar{r}} + \bar{u}^{(c)}_{\bar{z}})(1 - \bar{R}^2_{\bar{z}}) + 2(\bar{u}^{(c)}_{\bar{r}} - \bar{w}^{(c)}_{\bar{z}})\bar{R}_{\bar{z}}], \tag{2.6}$$

$$2\mu^{(c)}[\bar{u}^{(c)}_{\bar{r}} + \bar{w}^{(c)}_{\bar{z}}\bar{R}^2_{\bar{z}} + \bar{R}_{\bar{z}}(\bar{w}^{(c)}_{\bar{r}} + \bar{u}^{(c)}_{\bar{z}})] - 2\mu^{(a)}[\bar{u}^{(a)}_{\bar{r}} + \bar{w}^{(a)}_{\bar{z}}\bar{R}^2_{\bar{z}} + \bar{R}_{\bar{z}}(\bar{w}^{(a)}_{\bar{r}} + \bar{u}^{(a)}_{\bar{z}})]$$
$$= (-\bar{p}^{(a)} + \bar{p}^{(c)})(1 + \bar{R}^2_{\bar{z}}) - \gamma(1 + \bar{R}^2_{\bar{z}})\left(\frac{1}{\bar{R}(1 + \bar{R}^2_{\bar{z}})^{1/2}} - \frac{\bar{R}_{\bar{z}\bar{z}}}{(1 + \bar{R}^2_{\bar{z}})^{3/2}}\right) \tag{2.7}$$

are enforced, corresponding to the continuity of velocity, continuity of tangential stress and jump in normal stress according to the Young–Laplace law respectively. Here, γ denotes the surface tension. In addition, at the free surface the kinematic boundary condition,

$$\bar{u}^i = \bar{R}_{\bar{t}} + \bar{w}^i \bar{R}_{\bar{z}}, \tag{2.8}$$

must also be satisfied. Of course, physical significance requires that at the tube centreline the velocity field be finite, which provides an additional constraint for the core flow solutions.

The flow governed by the system (2.1)–(2.8) always admits an exact solution corresponding to flow with a flat interface, $\bar{R} = \bar{R}_0$,

$$\bar{w}^{(a)} = \frac{\bar{r}^2 - \bar{a}^2}{4\mu^{(a)}}(\bar{p}_{\bar{z}}^{(a)} + \rho^{(a)}g) + \frac{g\bar{R}_0^2}{2\mu^{(a)}}(\rho^{(c)} - \rho^{(a)})\log\left(\frac{\bar{r}}{\bar{a}}\right), \tag{2.9}$$

$$\bar{w}^{(c)} = \frac{\bar{r}^2 - \bar{R}_0^2}{4\mu^{(c)}}(\bar{p}_{\bar{z}}^{(c)} + \rho^{(c)}g) + \frac{\bar{R}_0^2 - \bar{a}^2}{4\mu^{(a)}}(\bar{p}_{\bar{z}}^{(a)} + \rho^{(a)}g) + \frac{g\bar{R}_0^2}{2\mu^{(a)}}(\rho^{(c)} - \rho^{(a)})\log\left(\frac{\bar{R}_0}{\bar{a}}\right), \tag{2.10}$$

where the only non-zero velocity component is the axial one, $\bar{w}$, and the only non-zero gradient is the radial one, $\partial_{\bar{r}}$. Here, the normal stress boundary condition (2.7) reduces to $\bar{p}_{\bar{z}}^{(a)} = \bar{p}_{\bar{z}}^{(c)} \equiv \bar{p}_{\bar{z}}$. This parallel-flow flat solution is a balance of viscous and gravitational forces and the imposed pressure gradient driving the core flow; an example of velocity profiles given by (2.9) and (2.10) is shown in figure 1(*b*). It should be noted that if $\bar{R}_0 = 0$, corresponding to the tube being entirely filled with the annular fluid, (2.9) reduces to the profile of Poiseuille pipe flow; likewise, if one sets $\bar{R}_0 = \bar{a}$, (2.10) reduces to that of Poiseuille flow of the core fluid.

The stability of the exact solution given by (2.9) and (2.10) was studied by Hickox (1971) for various values of the parameters of the problem (see also Yih 1967 for an analysis with a similar set-up without surface tension). In order to study the evolution of these interfacial disturbances and the flow of the annular film in the simplest possible setting, we turn to a model of the flow developed using long-wave asymptotics.

2.2. *Fully coupled long-wave equations*

The dimensional parameters μ^i, ρ^i, g, γ, $\bar{Q}^{(c)}$, $\bar{a}$, $\bar{R}_0$ and $\bar{\lambda}$, where $\bar{\lambda}$ denotes the length of a typical interfacial disturbance, combine to form seven dimensionless parameters: (i) Reynolds number *Re*, (ii) Froude number *Fr*, (iii) capillary number *C*, (iv) viscosity ratio *m*, (v) density difference ratio *l*, (vi) film thickness parameter *a* and (vii) aspect ratio ϵ, defined by

$$\left.\begin{array}{l} Re = \dfrac{2\rho^{(c)}\bar{Q}^{(c)}}{\pi\bar{R}_0\mu^{(c)}}, \quad Fr = \dfrac{2\bar{Q}^{(c)}}{\pi\bar{R}_0^{5/2}g^{1/2}}, \quad C = \dfrac{2\bar{Q}^{(c)}\mu^{(c)}}{\pi\gamma\bar{R}_0^2}, \\[3mm] m = \dfrac{\mu^{(a)}}{\mu^{(c)}}, \quad l = \dfrac{\rho^{(a)} - \rho^{(c)}}{\rho^{(c)}}, \quad a = \dfrac{\bar{a}}{\bar{R}_0}, \quad \epsilon = \dfrac{\bar{R}_0}{\bar{\lambda}}. \end{array}\right\} \tag{2.11}$$

The dynamics of the film flow is uniquely determined by the values of these seven dimensionless parameters. We note that other parameter choices are also valid. For instance, (2.11) corresponds to a viewpoint where the core volume flux $\bar{Q}^{(c)}$ and

mean film thickness $\bar{R}_0$ are prescribed, and the annular volume flux $\bar{Q}^{(a)}$ and pressure gradient respond accordingly. One could replace the aspect ratio a with a flux-ratio parameter $Q^{(a)} = \bar{Q}^{(a)}/\bar{Q}^{(c)}$, corresponding to a viewpoint where both fluid fluxes are prescribed and the mean film thickness and pressure gradients respond accordingly. Moreover, in other studies of core–annular flows the Weber number $We = C \times Re$ is sometimes used in place of the capillary number. Finally, we note that with the density ratio defined as in (2.11), the case where equal density fluids occupy the core and annular regions is defined by $l = 0$.

System (2.1)–(2.8) can be made dimensionless by typical scales

$$\left.\begin{array}{c} r = \bar{r}/\bar{R}_0, \quad z = \bar{z}/\bar{\lambda}, \quad u = \bar{u}/\overline{U}_0, \\ w = \bar{w}/\overline{W}_0, \quad t = \bar{t}\overline{W}_0/\bar{\lambda}, \quad p^i = \epsilon \bar{p}^i \bar{R}_0/(\mu^{(c)}\overline{W}_0), \end{array}\right\} \tag{2.12}$$

where $\overline{W}_0 = 2\bar{Q}^{(c)}/\pi \bar{R}_0^2$ is the core flow centreline velocity and $\overline{U}_0 \equiv \epsilon \overline{W}_0$. After substitution of (2.12) into (2.1)–(2.8), we consider first the leading order in an asymptotic expansion for the limit of the long-wave parameter $\epsilon \to 0$. In addition to small ϵ, we also restrict the values of Re by requiring that in the long-wave limit the limit $\epsilon Re \to 0$ as well. Under these assumptions, the motion equations (2.1)–(2.3) and boundary conditions (2.4)–(2.8) made dimensionless by (2.12) yield a leading-order velocity profile $w_{LW}^{(a)}$ and $w_{LW}^{(c)}$ given in appendix A by (A 1)–(A 2); this solution is a slowly varying z-dependent modulation of the exact parallel flow (2.9)–(2.10). The slowly varying annular pressure is now related to that of the core fluid by the asymptotic normal stress boundary condition (2.7)

$$p_z^{(a)} = p_z^{(c)} + \frac{1}{C}\left(\frac{1}{R} - \epsilon^2 R_{zz}\right)_z \tag{2.13}$$

at the long-wave interface $r = R(z, t)$. As is customary, while the second term R_{zz} in the capillary tension force balance expressed by (2.13) is formally of higher order, it is retained to account for uniform matched-asymptotics validity of the long-wave expansion (see, e.g., Oron *et al.* 1997).

Next, we seek approximate expressions for the pressure gradients p_z^i. These are found through the dimensionless volume fluxes

$$q^{(c)}(z, t) = 2\pi \int_0^R w_{LW}^{(c)} r \, dr, \quad q^{(a)}(z, t) = 2\pi \int_R^a w_{LW}^{(a)} r \, dr, \tag{2.14a,b}$$

which are given in expressions (A 3)–(A 4) in appendix A. Incompressibility of both core and annular fluids implies that the total volume flux $q^{(a)} + q^{(c)}$ through the tube is independent of the spatial location z. In the case where the volume flux $\bar{Q}^i$ of each fluid is prescribed at one end of the tube, the total flux anywhere in the tube is thus

$$q^{(a)}(z, t) + q^{(c)}(z, t) = Q^{(a)} + Q^{(c)}, \tag{2.15}$$

where the Q^i are the prescribed fluxes made dimensionless by $\overline{W}_0\bar{R}_0^2$. Then, with the free surface boundary condition (2.13), equations (A 3)–(A 4) determine the pressure terms $p_z^{(a)}$ and $p_z^{(c)}$ as functions of R and its spatial derivatives; $p_z^{(a)}$ is given in (A 5) in appendix A and $p_z^{(c)}$ is recovered through (2.13).

An evolution equation for $R(z, t)$ follows from volume conservation of either the core or the annular fluid and the kinematic boundary condition (2.8). Focusing for definiteness on the annular fluid, this equation can be expressed in terms of the annular flux as

$$\pi(a^2 - R^2)_t + (q^{(a)})_z = 0. \tag{2.16}$$

2.3. *Decoupled long-wave models*

Various model equations can be derived via different asymptotic balances between the parameters m, l, a, C and Re/Fr^2, and the free surface location R. The model equation derived in Camassa *et al.* (2012) is recovered when the additional asymptotic orderings $m \gg (a/\tilde{R})^4$ and $m \gg l(a/\tilde{R})^4$ are satisfied, where $\tilde{R}$ is a characteristic value for the core radius, and when $C = O(1)$ and $Fr^2 = O(Re)$. These asymptotic relations are realized by a high annular-to-core viscosity ratio and a core region that is not exceedingly small in volume (see appendix for a brief discussion of a model appropriate under a different asymptotic balance corresponding to 'very thick-film' problems studied elsewhere), and imply that $q^{(a)} \ll q^{(c)}$ so that the core fluid is moving much faster than the annular fluid. This difference in time scales for the two fluids allows the annular film flow to be decoupled from the core flow, in the sense that the core flow experiences the free surface essentially as a rigid wavy wall.

Under these assumptions, the pressure gradient $p_z^{(a)}$ simplifies to (A 8). Substitution of this approximate $p_z^{(a)}$ into (2.16) yields the model equation in Camassa *et al.* (2012) after a rescaling in time $t' = t/m$ (and immediately dropping the prime for ease of notation of the time derivative),

$$R_t + [f_1(R; a) - F(a)f_2(R; a)]R_z + \frac{S(a)}{R}[f_3(R; a)(R_z + R^2 R_{zzz})]_z = 0, \qquad (2.17)$$

where the functions f_n, $n = 1, 2, 3$, are given by

$$\left.\begin{aligned}
f_1(R; a) &= \frac{a^2}{R^4}\left(\frac{a^2}{R^2} - 1\right), \\
f_2(R; a) &= a^2 - R^2 - 2R^2 \log\left(\frac{a}{R}\right), \\
f_3(R; a) &= \frac{a^4}{R^2} - 4a^2 + 3R^2 + 4R^2 \log\left(\frac{a}{R}\right)
\end{aligned}\right\} \qquad (2.18)$$

and the parameters F and S by

$$F(a) = \frac{Re\, l}{2Fr^2}, \quad S(a) = \frac{1}{16C}. \qquad (2.19a,b)$$

Here, $R(z, t) = \bar{R}/\bar{R}_0$ is the dimensionless radial location of the interface as a function of axial location and time, where $\bar{R}_0$ is the mean radius of the core region, and $a = \bar{a}/\bar{R}_0$ is the dimensionless tube radius. The parameter F represents the ratio of the free surface stress created by the core flow to gravity and S is the inverse of a capillary number. We have also adopted the convention of returning to the original aspect ratio by rescaling z and t by ϵ as in Camassa *et al.* (2012). This results in ϵ being scaled out of (2.17), but the validity of the model equation still depends on the condition $\epsilon \ll 1$ being satisfied.

Equation (2.17) is strongly nonlinear, i.e. no smallness assumption on the free surface displacement from a reference flat configuration has been made. Moreover, the model retains the cylindrical geometry of the problem, as evidenced by the inverse powers and logarithms of R.

The dynamics of the governing equations was determined by seven dimensionless parameters, while the dynamics of (2.17) is determined by three parameters: F, which represents the competition between viscous forces at the interface and gravity forces;

S, which keeps track of the competition between viscous forces at the interface and stresses from capillary forces; and a, the film thickness parameter. Both S and F are dependent on the thickness of the film. All three parameters play a role in determining whether nonlinear disturbances to the free surface travel upwards or downwards. As we will see, the weakly nonlinear regime is somewhat simpler in that the direction of disturbance propagation is determined only by F and a. Specifically, if $F < f_1(1; a)/f_2(1; a)$ disturbances travel up the tube, i.e., the free surface stress caused by the core flow dominates the effects of gravity, otherwise disturbances travel downward due to gravity overpowering the effects of the core flow.

It should be noticed that F and S depend on the film thickness parameter a through the Reynolds, Froude and capillary numbers as a result of the choice of length scales used to define these parameters. An alternative choice for parameters which would remove the a dependence from F and S and incorporate it into the functions f_n may be preferable, i.e. define new coefficients $\tilde{F} = a^4 F$ and $\tilde{S} = a^2 S$ which would correspond to $\tilde{f}_2 = a^{-4} f_2$ and $\tilde{f}_3 = a^{-2} f_3$. This choice makes the coefficients F and S independent of film thickness initial data and thus constant across different realizations of an experiment with fixed 'hardware' set-up μ^i, ρ^i, $\bar{Q}^{(c)}$, $\bar{a}$ and γ. However, to be consistent with previous literature, we follow the definitions given in (2.19) for the rest of this work.

In the case of equal densities of the core and annular fluid (or negligible gravity), i.e. $F = 0$, (2.17) reduces to the model equation derived by Camassa & Lee (2006) up to a choice of scalings:

$$R_t + f_1(R; a)R_z + \frac{S(a)}{R}[f_3(R; a)(R_z + R^2 R_{zzz})]_z = 0. \tag{2.20}$$

For ease of reference, it is worth labelling these two models with easily identifiable tags. Thus, in the following we will refer to the long-wave models (2.17) and (2.20) as (LW-PG) and (LW-P) respectively.

2.4. *Thin-film models*

If the liquid film is thin, further simplifications of (LW-PG)/(2.17) and (LW-P)/(2.20) can be expected. We recall the non-dimensional scaling $a = \bar{a}/\bar{R}_0$ and $R = \bar{R}/\bar{R}_0$: the limit of thin films corresponds to $\bar{R}_0 \to \bar{a}$, so that a limits to 1 from above and the spatial mean of the non-dimensional interface position R also limits to unity. The thin-film limit asymptotics can then be described by a thinness small parameter $0 < \beta \ll 1$, where $a = 1 + \beta$, and by shifting to a new dependent variable $h(z, t)$, with spatial mean 1, defined by

$$R = 1 + \beta(1 - h), \tag{2.21}$$

so that βh represents the non-dimensional height of the interface measured from the tube wall (i.e. the thickness of the annular film). Then, (LW-PG)/(2.17) can be rewritten in terms of h, and each of the functions f_n, $n = 1, 2, 3$, in (LW-PG) can be expanded about $\beta = 0$:

$$\left.\begin{aligned} f_1 &= 2h\beta + (-6h + 11h^2)\beta^2 + (12h - 44h^2 + 36h^3)\beta^3 + O(\beta^4), \\ f_2 &= 2h^2\beta^2 \left(1 - \frac{h\beta}{3}\right) + O(\beta^4), \\ f_3 &= \frac{16h^3}{3}\beta^3 + O(\beta^4). \end{aligned}\right\} \tag{2.22}$$

Notice that the order of the gravity term is $f_2 = O(\beta^2)$, while the order of the core flow term is $f_1 = O(\beta)$. Thus, asymptotically the effects of tangential stress at the interface dominate the effects of gravity in the thin-film limit. Notice also that the effects of surface tension are of order $O(\beta^3)$; these effects are again typically retained despite their higher order for reasons discussed in, e.g., Camassa *et al.* (2014). Substituting the expanded f_n into the long-wave model (LW-PG) and retaining up to $O(\beta^2)$ hyperbolic terms (while retaining the $O(\beta^3)$ term of f_3 to keep the effects of surface tension) gives

$$h_t + hh_z + \tilde{F}h^2 h_z + \tilde{S}^*[h^3(h_z + h_{zzz})]_z = 0, \qquad (2.23)$$

where $\tilde{F} = \beta(11 - 2F)/(2 - 6\beta)$ and $\tilde{S}^* = 8\beta^2 S/[3(1 - 3\beta)]$, and time has been rescaled by $t' = (2\beta - 6\beta^2)t$ (again having dropped primes).

If the densities of the two fluids are equal or the effects of gravity are negligible, i.e. $F = 0$, then substitution of (2.22) into (2.17) and retention of only the $O(\beta)$ hyperbolic terms results in the standard form of the thin-film model for pressure-driven flow (after a rescaling in time by $t' = 2\beta t$, dropping primes hereafter),

$$h_t + hh_z + \tilde{S}[h^3(h_z + h_{zzz})]_z = 0, \qquad (2.24)$$

where $\tilde{S} = 8\beta^2 S/3$. Equation (2.24) is the thin-film counterpart to the long-wave model (LW-P)/(2.20) and was derived directly from the governing equations and studied numerically by Kerchman (1995). For models (2.23) and (2.24), we will use, respectively, the tags (TF-PG) and (TF-P).

While a study of the general dynamical features of all the above models has to rely in large part on their numerical simulations, much insight can be gained by analysing special solutions such as travelling waves, or by studying transient growth of perturbations from exact simple solutions such as those corresponding to a flat interface, thereby determining their linear stability. We will use all these tools, starting with linearized dynamics, next.

3. Linear stability analysis

We now analyse the linear stability of simple (flat) exact solutions for both pressure-driven flow with negligible gravity (LW-P) and (TF-P), and the full equations (LW-PG) and (TF-PG). A small perturbation to the free surface is introduced to each model,

$$R = 1 + A \exp[i(kz - \omega t)], \quad h = 1 + \tilde{A} \exp[i(kz - \omega t)], \qquad (3.1a,b)$$

where $A \ll 1$ or $\tilde{A} \ll 1$ is the amplitude of the disturbance, k is its wavenumber and ω is the temporal frequency. The dispersion relation obtained from substitution of (3.1) into each model equation will first be examined from a temporal viewpoint. The instabilities will then be classified as absolute or convective.

3.1. *Pressure-driven flow*

Introduction of the perturbation (3.1) into the pressure-driven model equations (LW-P) and (TF-P) yields the dispersion relations

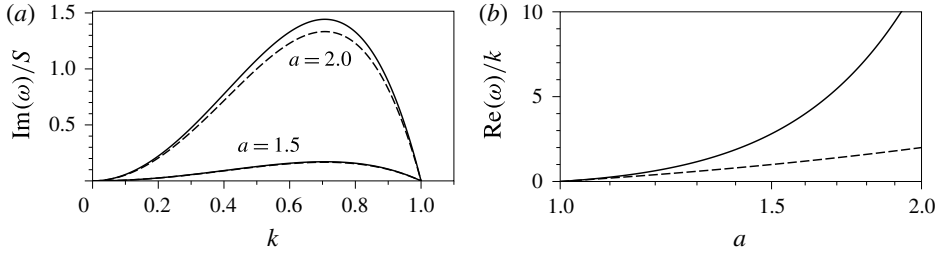$$\omega_{LW\text{-}P} = (a^4 - a^2)k + iS(a^4 - 4a^2 + 3 + 4\log a)(k^2 - k^4), \qquad (3.2)$$

FIGURE 2. (*a*) Growth rates of (LW-P) (solid lines) and (TF-P) (dashed lines) for two values of *a*. (*b*) Speed of linear perturbations as a function of *a*.

$$\omega_{TF\text{-}P} = 2(a-1)k + \frac{16\mathrm{i}(a-1)^3 S}{3}(k^2 - k^4). \tag{3.3}$$

(It should be noted that (3.3) corresponds to (TF-P) prior to a rescaling of time by 2β.)

The maximum growth rate of each model occurs for disturbances with wavenumber $k_m = 1/\sqrt{2}$, corresponding to a (dimensional) wavelength of $\bar\lambda_m = 2\pi\sqrt{2}\bar R_0$, indicating that the typical wavelength of disturbances is set by the radius of the interface, in analogy to the classical result for jets due to Rayleigh. The maximum growth rate for each model is given by

$$\mathrm{Im}[\omega_{LW\text{-}P}]|_{k_m} = \frac{S}{4}(a^4 - 4a^2 + 3 + 4\log a), \tag{3.4}$$

$$\mathrm{Im}[\omega_{TF\text{-}P}]|_{k_m} = \frac{4S}{3}(a-1)^3. \tag{3.5}$$

Figure 2(*a*) shows the growth rates of each model for two values of *a*. The models are in close agreement with one another, with model (TF-P) producing slightly smaller growth rates. The real part of each dispersion relation describes the propagation speed of infinitesimal interfacial disturbances. Figure 2(*b*) shows the phase speeds for each model as a function of the film thickness parameter *a*; disturbances in the thin-film model travel slower than those in the long-wave model.

We remark that both dispersion relations (3.2) and (3.3) are, to within a choice of scaling, identical to the well-known Kuramoto–Sivashinsky (KS) equation (see, e.g., Kuramoto & Tsuzuki 1980, Sivashinsky & Michelson 1980 or Kerchman 1995). Variants of the KS equation have been used to model weakly nonlinear thin films, and solutions to the KS equation are known to exhibit spatio-temporal chaos; we return briefly to this in § 4.

Since solutions to both models are unstable to a range of small wavenumbers *k*, we now examine whether solutions to each model are convectively or absolutely unstable. This classification of instabilities is borrowed from the literature concerning jets, and has been studied in the case of gravity-driven film flows which coat tubes, e.g. Duprat *et al.* (2007) for exterior gravity-driven liquid coatings and Camassa *et al.* (2014) for interior gravity-driven liquid coatings; see also Vellingiri, Tseluiko & Kalliadasis (2015) for a study of absolute and convective instabilities in the related problem of gas–liquid film flows in a channel geometry. It was shown by Duprat *et al.* (2007) that there is a simple criterion for determining whether solutions to (5.3)

are absolutely or convectively unstable using the method developed by Briggs (1964) and Bers (1983), and expanded by Huerre & Monkewitz (1990).

The criterion for absolute instability in the Frenkel model (5.3) (Frenkel 1992; also see § 5 for further discussion of its relation to the core–annular models) was found by Duprat *et al.* (2007) to be

$$S' > \frac{3(-17 + 7\sqrt{7})^{1/2}}{16(a-1)^2}. \tag{3.6}$$

Since the dispersion relation for the Frenkel equation,

$$\omega_F = -2(a-1)^2 k + \frac{16\mathrm{i}S'(a-1)^3}{3}(k^2 - k^4), \tag{3.7}$$

can be transformed into (3.3) by the transformation $\omega_F = -2(a-1)\omega_{TF\text{-}P}$ and $S' = -(a-1)S$, we find that interfacial perturbations to model (TF-P) are absolutely unstable if the following condition is satisfied (after a sign change to account for the different direction of disturbance propagation):

$$S > \frac{3(-17 + 7\sqrt{7})^{1/2}}{16(a-1)^2}. \tag{3.8}$$

Alternatively, this condition can be expressed as a condition on the dimensional film thickness:

$$\bar{h}_0 \equiv \bar{a} - \bar{R}_0 > \left[\frac{6\bar{Q}^{(c)}\mu^{(c)}(-17 + 7\sqrt{7})^{1/2}}{\pi\gamma} \right]^{1/2}. \tag{3.9}$$

If condition (3.9) is not satisfied, the free surface is convectively unstable.

The thin-film dispersion relation (3.3) can be transformed into (3.2) by the transformation

$$\omega_{TF\text{-}P} = \frac{2(a-1)}{a^4 - a^2}\omega_{LW\text{-}P} \quad \text{and} \quad S = \frac{3(a^4 - 4a^2 + 3 + 4\log a)}{8(a-1)^2(a^4 - a^2)}S^*. \tag{3.10a,b}$$

Thus, the condition for interfacial disturbances to be absolutely unstable in the long-wave model is (immediately dropping asterisks)

$$S > \frac{(-17 + 7\sqrt{7})^{1/2}(a^4 - a^2)}{2(a^4 - 4a^2 + 3 + 4\log a)}. \tag{3.11}$$

Figure 3 shows the regions of S–a parameter space for which interfacial disturbances are absolutely unstable for each model. While both models are convectively unstable for small S and absolutely unstable for large S, there is an intermediate range of S values for which disturbances in the thin-film model are absolutely unstable while disturbances in the long-wave model are only convectively unstable. This is perhaps to be expected from the results in figure 2. The thin-film model's growth rate is slower than its long-wave counterpart (recall that $a > 1$ for fluid coating the interior of a tube), which intuitively would decrease the region of parameter space in which absolute instabilities are found. However, figure 2(*b*) shows that the phase speed for the thin-film case is smaller than its long-wave counterpart, and this could be expected to have the opposite effect of increasing the region of absolute instability for model (TF-P). The results in figure 3 indicate that the lower phase speed is the dominant factor in determining the nature of instabilities; this also agrees with the relatively large difference in phase speeds and small difference in growth rates between the models, as seen in figure 2, for values of the radius a sufficiently larger than unity.
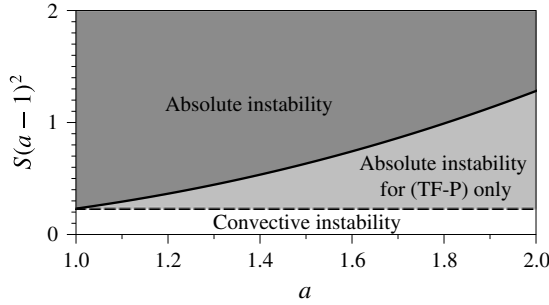
FIGURE 3. Shaded regions of *S*–*a* parameter space indicating interfacial disturbances that are absolutely unstable for (TF-P) only (light grey) or both (LW-P) and (TF-P) (dark grey).

3.2. *Full equations*

We now briefly repeat the linear stability analysis for the full model equations. Introduction of perturbations (3.1) into the long-wave and thin-film models (LW-PG) and (TF-PG) respectively yields the dispersion relations

$$\omega_{\text{LW–PG}} = [a^4 - a^2 - (a^2 - 1 - 2\log a)F]k + \mathrm{i}S(a^4 - 4a^2 + 3 + 4\log a)(k^2 - k^4), \quad (3.12)$$

$$\omega_{\text{TF–PG}} = [2(a-1) + (a-1)^2(5 - 2F)]k + \frac{16\mathrm{i}(a-1)^3 S}{3}(k^2 - k^4). \quad (3.13)$$

The maximum growth rates of each model are identical to (3.4) and (3.5); the wavelengths k_m of maximum growth rate are also unchanged by the addition of the gravity term. The influence of gravity is seen solely in the speed of disturbances through the real part of each dispersion relation. Figure 4(*a*) shows the speed of disturbances in each model as a function of *a* for two values of *F*. For each model there is a critical value $F_c(a)$ for which the effects of gravity and surface stress balance one another so that disturbances remain in a fixed location as long as their growth remains in the linear regime. For $F > F_c$ (gravity stronger than surface stress), linear disturbances move down the tube, and for $F < F_c$ (gravity weaker), disturbances move up the tube. For the long-wave and thin-film models these critical values are, respectively, $F_{c_{LW}} = (a^4 - a^2)/(a^2 - 1 - 2\log a)$ and $F_{c_{TF}} = (5a - 3)/(2a - 2)$ (these values are shown in figure 4*b*). It should be noted that the thin-film model once again predicts lower velocities than the long-wave model, which is consistent with both the pressure-driven subcase of speed in model (TF-P) being lower than its long-wave counterpart and the gravity-driven subcase where the appropriate model (5.3) predicts higher (downward) speed than its long-wave counterpart as in Camassa *et al.* (2014).

The dispersion relation (3.3) can be transformed into (3.13) by a similar transformation to those in § 3.1. The condition for interfacial disturbances to be absolutely unstable in the thin-film model (TF-PG) is then

$$S > \left| \frac{3(-17 + 7\sqrt{7})^{1/2}[2(a-1) + (a-1)^2(5 - 2F)]}{32(a-1)^3} \right|. \quad (3.14)$$

The absolute value bars in (3.14) are necessary since, for $F > 2.5$, there is a range of large enough *a* for which the speed of instabilities will be negative, due to the effects of gravity being stronger than the interfacial stress from the core flow. For given *F*
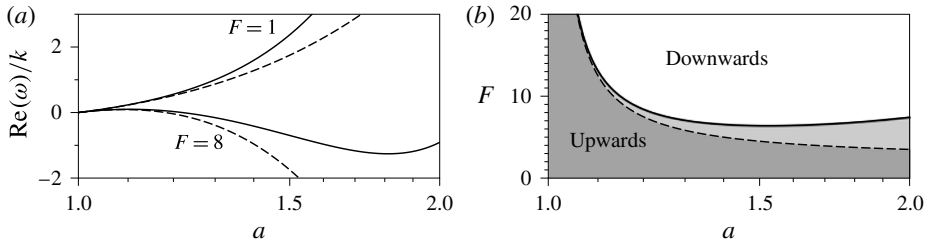
FIGURE 4. (*a*) Speed of an infinitesimal disturbance to (LW-PG) (solid line) and (TF-PG) (dashed line) for two values of *F*; (*b*) $F = F_{c_{LW}}$ (solid line) and $F = F_{c_{TF}}$ (dashed line) for (LW-PG) and (TF-PG) respectively, distinguishing between upwards and downwards flow of linear disturbances.
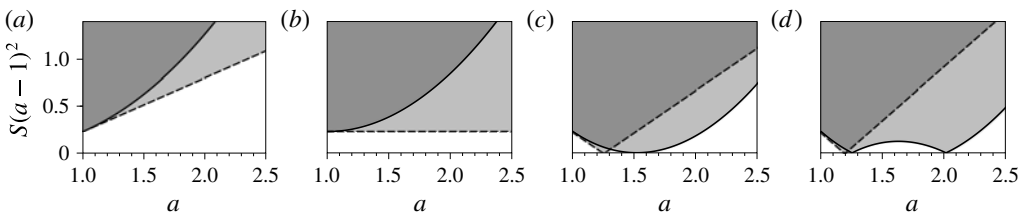

FIGURE 5. Shaded regions of *S*–*a* parameter space indicating interfacial disturbances that are absolutely unstable for only one of (light grey) or both (dark grey) (LW-PG) and (TF-PG) for four different values of *F* (1.0 (*a*), 2.5 (*b*), 5.0 (*c*), 7.5 (*d*)).

in the range $F > 2.5$ there is exactly one value of *a*, specifically $a = (2F - 3)/(2F - 5)$, for which the right-hand side of (3.14) vanishes, indicating that disturbances are absolutely unstable for any *S*; this is due to the effects of gravity and interfacial stress exactly cancelling one another.

The long-wave model's dispersion relation (3.12) can be recovered from (3.13) by yet another transformation; this leads to the following condition for absolute instability in the long-wave model (LW-PG):

$$S > \left| \frac{(-17 + 7\sqrt{7})^{1/2}[a^4 - a^2 - (a^2 - 1 - 2\log a)F]}{2(a^4 - 4a^2 + 3 + 4\log a)} \right|. \tag{3.15}$$

Figure 5 shows the regions in *S*–*a* parameter space for which disturbances are absolutely unstable for four values of *F*. For small values of *F*, the long-wave model predicts convective instability for more parameter combinations than the thin-film model. For larger values of *F*, there is a range of *a* in which the long-wave model predicts absolute instability for more parameter combinations than the thin-film model. Unlike the thin-film model, for every *F* in the range $F > 6.391$ there are exactly two values of *a* for which any value of *S* results in absolute instability.

4. Numerical solutions

The process of saturation of the instabilities discussed in the previous section, beyond their initial transients, does not seem to be amenable to an analytical approach and must be studied numerically. In this section, both transient solutions and travelling

wave solutions to the pressure-driven models (TF-P) and (LW-P) are presented. The two models' transient solutions display qualitatively different interactions between nonlinear free surface waves, while the travelling wave solutions, when viewed in a travelling reference frame, exhibit two distinct flow regimes, one in which a region of recirculating fluid exists near the wave crest and one in which no such region is found.

4.1. *Transient solutions*

We first seek solutions to the model equations (TF-P) and (LW-P) with periodic boundary conditions. Numerical integration of each equation is achieved by a pseudospectral method, whereby spatial derivatives and nonlinearities are calculated in Fourier and physical space respectively. A simple second-order predictor–corrector scheme for time integration is used. Due to the nonlinearities in all the models, the Fourier coefficients are appropriately dealiased. The conserved quantities R^2 or h are monitored throughout the simulations. For initial conditions, the flat free surface is perturbed with either a single mode or multiple modes, i.e. $h(z, 0) = 1 + \sum_{k=1}^{n} \delta_k \cos(2\pi k z + \alpha_k)$, where α_k is a random phase shift for each mode. See Camassa *et al.* (2012), Ogrosky (2013) or Camassa *et al.* (2014) for more details on the numerical simulations.

Figure 6(*a–c*) contains series of snapshots showing the evolution of a slightly perturbed interface for long-wave model (LW-P) with various values of S and a; figure 6(*a*) shows a relatively thick film ($a = 1.25$) and figure 6(*c*) shows a much thinner film ($a = 1.05$). The values of S were chosen in such a way that all three correspond to the thin-film case where $\tilde{S} = 0.3$ in order to make a direct comparison with the dynamics of solutions to equation (TF-P). In addition, the initial conditions were identical, i.e. each δ_k and α_k used in one simulation was identical to those used in every other simulation; the scaling for the initial condition $h(z, 0)$ is shown to the right of figure 6(*d*). Instabilities propagate up the tube, shown here from left to right; it should be noted that successive snapshots are displayed here in a frame of reference moving with the speed of the undisturbed interface. Unlike the case of gravity-driven flow studied in Camassa *et al.* (2014), in no simulations of (LW-P) did we observe unchecked amplitude growth in finite time (corresponding to 'choking' of the core fluid). This highlights the coupling between the core flow and the annular flow through the stress at the free surface; the effect of a growing instability on the hyperbolic term (through the increase in free surface stress) prevents blowup. This is in line with behaviour seen in experiments conducted in Camassa *et al.* (2012): at high core volume fluxes $\bar{Q}^{(c)}$ the rapid increase in the speed of the core fluid in order to pass through a constricted opening prevents plug formation. We also remark that the slight depression in front of each wave, and the corresponding fore–aft asymmetry, is noticeable in all the wave forms in our simulations. This feature is shared among wave solutions to long-wave, thin-film, flat-film and integral models, and it is even observed in simulations of propagating liquid plugs; see, e.g., Campana *et al.* (2007) and Ubal *et al.* (2008).

In figure 6(*a–c*), the free surface undergoes a period of instability growth governed by the linear analysis discussed in § 3. In figure 6(*a*), the free surface then exhibits spatio-temporal chaotic behaviour, reminiscent of solutions to the Kuramoto–Sivashinsky equation. Indeed, all the models considered here reduce to some form of the KS equation in the limit of weakly nonlinear disturbances. In figures 6(*b*) and 6(*c*), instabilities grow into the strongly nonlinear regime where a
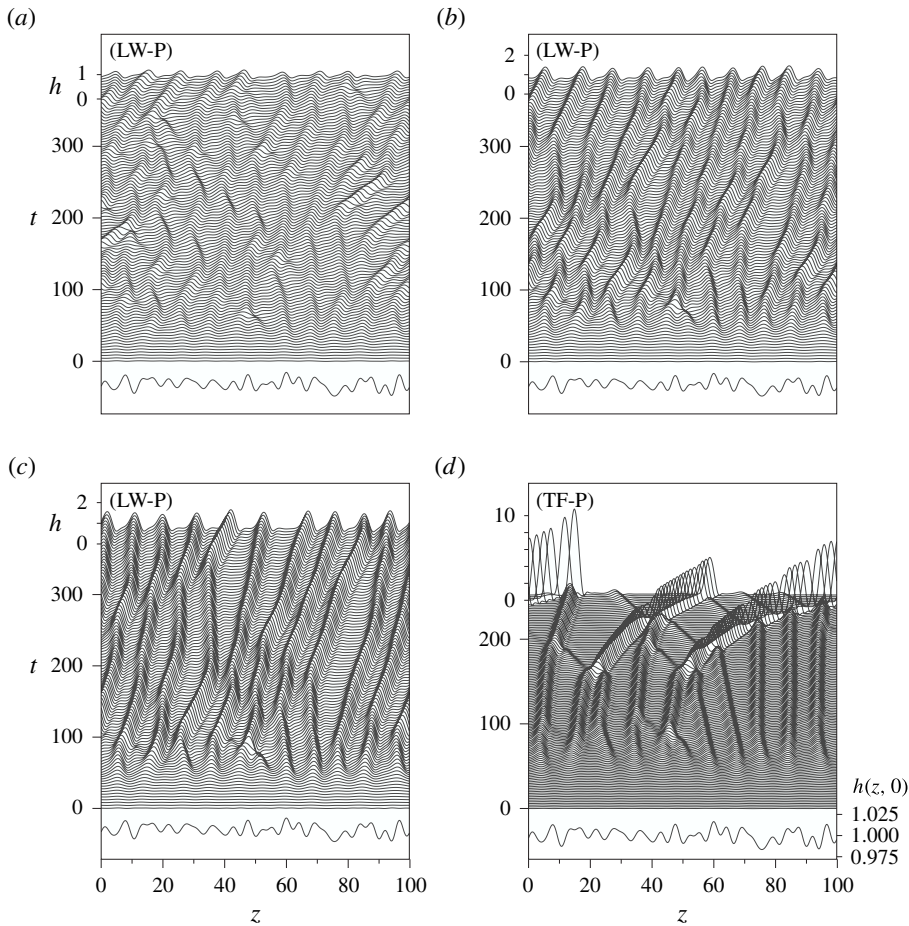
FIGURE 6. (*a–c*) Time snapshots showing the evolution of the free surface for (LW-P) in a periodic domain with (*a*) $S = 1.8$ and $a = 1.25$, (*b*) $S = 11.25$ and $a = 1.1$, and (*c*) $S = 45$ and $a = 1.05$. Free surface profiles are shown successively shifted at equal time intervals. Profiles are shown in the frame of reference moving with an undisturbed interface. (*d*) Solution to (TF-P) is shown for $\tilde{S} = 0.3$, which corresponds to each combination of S and a used in (*a*)–(*c*). Shown below each snapshot is the initial condition $h(z, 0)$; its scale is shown to the right in (*d*). Note the different time and amplitude scales of (*d*) with respect to the other panels.

nonlinear balance of forces allows the formation of more coherent wave motion. The waves propagate up the tube while undergoing nonlinear interactions with one another, eventually settling into a steady wavetrain. The effect of dispersive terms in KS-like equations has been shown to be regularizing, leading to the formation of travelling waves, see, e.g., Chang, Demekhin & Kopelevich (1993), Ogawa (1993) and Johnson *et al.* (2012). Because of this, it is perhaps to be expected that solutions to the fully nonlinear models (LW-P) and (TF-P) saturate to a coherent travelling wave regime.

Figure 6(*d*) shows the evolution of a perturbed interface for thin-film model (TF-P), for the parameter choice $\tilde{S} = 0.3$. There is a period of wave collisions and mergers following the initial instability growth, but unlike the evolution depicted for the long-
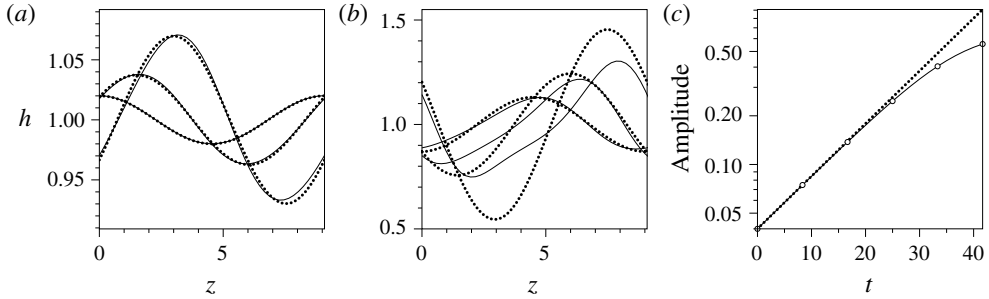
FIGURE 7. Snapshots of a single wave growing according to the linear theory of (3.2) (dotted line) and the nonlinear model (LW-P) (solid line) at (*a*) $t = 0$, 8.3, 16.7 and (*b*) $t = 25$, 33.3, 41.7 with $S = 11.25$ and $a = 1.1$. (*c*) The amplitude (distance between wave crest and trough) of the linear theory and strongly nonlinear model. Circles correspond to the model solutions shown in (*a*) and (*b*).

wave model, the largest wave consumes all others it overtakes. Kerchman (1995) found this to be the case in all his simulations with $0.15 < \tilde{S} < 1.0$ (see figures 4 and 5 in Kerchman 1995 for results with different values of $\tilde{S}$ in this range). Thus, even for relatively thin films, i.e. $a = 1.05$, the behaviour of the thin-film model solutions is qualitatively different from its counterpart in the corresponding long-wave model. This difference in solution behaviour can be attributed to the thin-film model's lack of memory of the tube's centreline. As the annular fluid waves grow in the long-wave model, impinging on the core region, the core fluid moves faster to maintain a constant volume flux. The additional stress caused by the increased velocity of the core fluid contributes to the nonlinear balance of travelling wave solutions through the hyperbolic term $f_1(R; a)R_z$. It should be noted that for $R \ll 1$ this term behaves like $R^{-6}R_z$. In the thin-film model there is no memory of the centreline of the tube, and instabilities can grow unchecked until they exhaust the supply of fluid in the rest of the domain. Only then, due to conservation of h, do the instabilities saturate.

In figure 7, the initial period of instability growth shown in figure 6(*b*) is compared with the linear theory of (3.2). A single wavelength with wavenumber closest to $k_m = 1/\sqrt{2}$ while still fitting in the periodic domain is shown at equally spaced time intervals in figure 7(*a*,*b*). For times $t < 25$ the growth is in excellent agreement with the linear theory. Figure 7(*c*) shows the amplitude (trough to crest) of the wave during this initial period of growth.

4.2. *Travelling wave solutions*

The numerical simulations show evidence of the dominant role played by travelling waves in most time evolutions governed by some of the models. As they are easily computable numerically with any desired accuracy, travelling wave solutions can thus be used to further expose the different mathematical and physical features exhibited by the models described in § 4.1, and to explore the kinematics of the underlying fluid, which is relevant for studying transport phenomena in these flows.

We once again focus here on the case of pressure-driven flow without gravity. Moving to a frame of reference travelling with the wave, i.e. letting
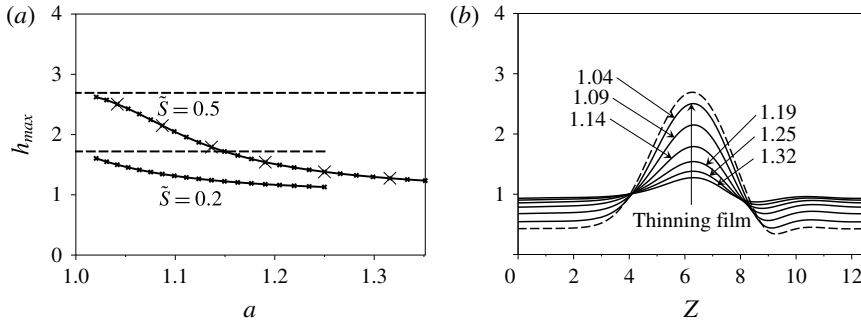
$$Z = z - ct, \tag{4.1}$$

FIGURE 8. (*a*) Maximum value of *h* attained in travelling wave solutions of (LW-P) and (TF-P) for various values of $\tilde{S}$ and *a*. (*b*) Solutions to the long-wave model (LW-P) for $\tilde{S} = 0.5$ are plotted (solid lines) for various values of *a*. The solution to the thin-film model (TF-P) for $\tilde{S} = 0.5$ is plotted (dashed line). The crosses in (*a*) correspond to profiles shown in (*b*).

and substituting (4.1) into the long-wave (LW-P) and thin-film (TF-P) models yields fourth-order ordinary differential equations (ODEs)

$$cR' = f_1(R; a)R' + \frac{S}{R}\frac{\mathrm{d}}{\mathrm{d}Z}[f_3(R; a)(R' + R^2 R''')], \tag{4.2}$$

$$ch' = hh' + \tilde{S}\frac{\mathrm{d}}{\mathrm{d}Z}[h^3(h' + h''')] \tag{4.3}$$

respectively. As neither (4.2) or (4.3) is solvable analytically, we seek solutions numerically as in Camassa *et al.* (2012). We do so by providing an initial guess, via a long-time simulation of the model PDEs, to an iteration scheme to solve a boundary value problem. Specifically, we let the time-dependent simulations settle to a steady series of travelling waves, from which a single wave form can be 'clipped'. This wave is then used as an initial approximation, within an appropriate domain, to be refined with a collocation method for a two-point boundary value problem solver.

Figure 8(*a*) shows the amplitude (maximum value of *h*) of travelling wave solutions to the long-wave model (LW-P) and thin-film model (TF-P) for two values of $\tilde{S}$ and various values of *a*. The long-wave model predicts wave amplitudes smaller than those of the thin-film model; even for moderate values of *a* this difference is significant. Figure 8(*b*) shows several of the travelling wave solutions for $\tilde{S} = 0.5$. As expected, in the thin-film limit $a \rightarrow 1$ the long-wave model solutions approach the waveform of their thin-film model counterparts.

Next, we investigate the effect of period cell length on solutions for each model class. Figure 9 depicts travelling waves for five different period cell lengths for (*a*) the long-wave model (LW-P) and (*b*) the thin-film model (TF-P). As the period cell length increases in the long-wave model, the geometry of the tube restricts growth of the wave amplitude. In model (TF-P) the wave amplitude grows roughly proportionally to the cell length, as shown by Kerchman (1995) (see figure 10 in Kerchman 1995 for similar growth with a different value of $\tilde{S}$). This is consistent with the model solution behaviour described in §4.1: in the thin-film model (TF-P), instability growth is bounded by mass conservation, while growth in model (LW-P) is only bounded primarily by mass conservation for very thin films, with thicker film
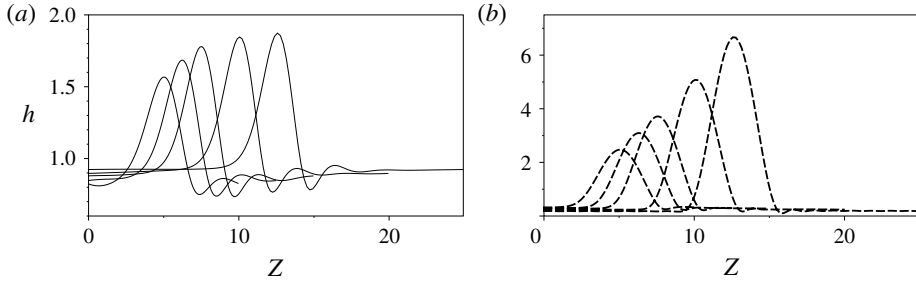
FIGURE 9. Various wavelength travelling wave solutions to (*a*) the long-wave model (LW-P) with $S = 4.17$ and $a = 1.25$, and (*b*) the thin-film model (TF-P) with $\tilde{S} = 1.0$. The mean film thickness has been normalized to $h_0 = 1$.

growth being bounded primarily by the core fluid's increased velocity. This difference has implications for the thickness of the substrate layer outside the wave crest as well; in the long-wave model, as the cell length increases and the geometry restricts the growth of the wave, the substrate layer increases in thickness to accommodate the additional liquid that the increasing cell length introduces. This effect is missed by the thin-film model where the waves are allowed to grow unbounded in amplitude; in fact, the substrate layer slightly decreases in thickness with increasing cell length.

It is instructive to view these differences between travelling wave solutions of the two model classes by monitoring the nonlinear balance of the terms in (4.2) and (4.3), reported here for convenience after taking the overall derivatives as

$$\sum_{i=1}^{6} g_i(Z) = 0, \quad \sum_{i=1}^{6} \tilde{g}_i(Z) = 0 \qquad (4.4a,b)$$

respectively, where

$$\left.\begin{array}{ccc} g_1 = -cR', & g_2 = f_1 R', & g_3 = \dfrac{S}{R} f_3 R'', \\[2mm] g_4 = \dfrac{S}{R} f_3 R'''', & g_5 = \dfrac{S}{R}(R')^2 \dfrac{\mathrm{d}}{\mathrm{d}R} f_3, & g_6 = \dfrac{S}{R} R' R''' \dfrac{\mathrm{d}}{\mathrm{d}R} f_3 \end{array}\right\} \qquad (4.5)$$

and

$$\left.\begin{array}{ccc} \tilde{g}_1 = -ch', & \tilde{g}_2 = hh', & \tilde{g}_3 = \tilde{S}h^3 h'', \\[2mm] \tilde{g}_4 = \tilde{S}h^3 h'''', & \tilde{g}_5 = 3\tilde{S}h^2(h')^2, & \tilde{g}_6 = 3\tilde{S}h^2 h' h'''. \end{array}\right\} \qquad (4.6)$$

In each of these ODEs, the first two terms give the hyperbolic contributions, the third and fourth terms give the weakly nonlinear contributions due to capillary forces and the final two terms give the strongly nonlinear capillary contributions. Figure 10(*a*) shows the profile of a solution to both equations (4.4) for $\tilde{S} = 0.5$. The contribution of each of the six terms $\tilde{g}_i(Z)$, $1 \leqslant i \leqslant 6$, to the solution of the thin-film equation in (4.4) is shown in figure 10(*b*) and the contribution of each of the six terms $g_i(Z)$ to the solution of the long-wave equation in (4.4) is shown in figure 10(*c*).
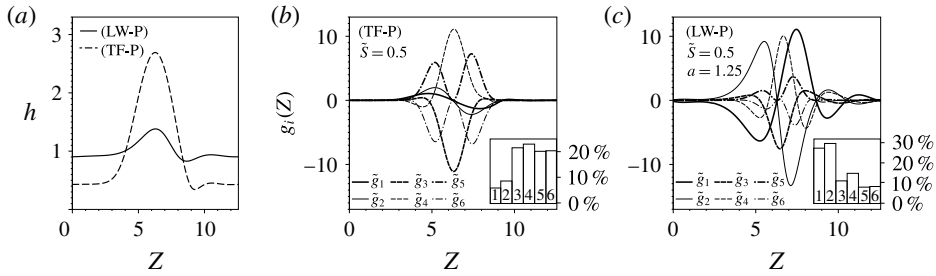
FIGURE 10. (*a*) Travelling wave solution to the long-wave model (LW-P) and the thin-film model (TF-P) for $\tilde{S} = 0.5$. (*b*) Contributions of the six terms $g_i(Z)$ for the thin-film model solution shown in (*a*). The inset shows the percentage contribution e_i defined in (4.7). (*c*) Contributions of the six terms $g_i(Z)$ for the long-wave model solution shown in (*a*).
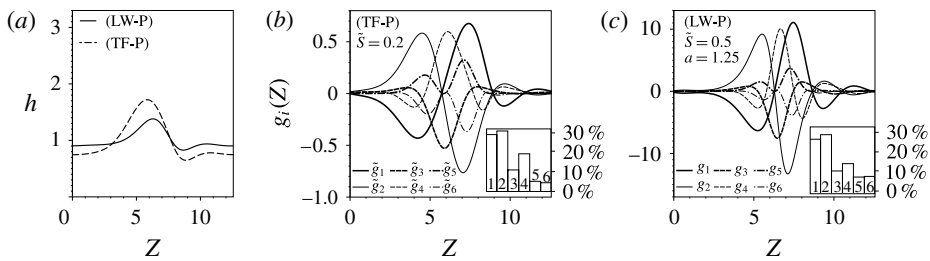

FIGURE 11. (*a*) Travelling wave solution to the long-wave model (LW-P) for $\tilde{S} = 0.5$ and the thin-film model (TF-P) for $\tilde{S} = 0.2$. (*b*) Contributions of the six terms $g_i(Z)$ for the thin-film model solution shown in (*a*). The inset shows the percentage contribution e_i defined in (4.7). (*c*) Contributions of the six terms $g_i(Z)$ for the long-wave model solution shown in (*a*).

The relative contribution of each term $\tilde{g}_i(Z)$ in the thin-film model (4.4) can be assessed by evaluating their mean contributions

$$e_i \equiv \int_0^L |\tilde{g}_i(Z)| \, \mathrm{d}z \bigg/ \sum_{i=1}^6 \int_0^L |\tilde{g}_i(Z)| \, \mathrm{d}z, \quad i = 1, \ldots, 6, \tag{4.7}$$

where L is the solution domain length; this gives a percentage measure of the overall contribution of each term to the solution across the domain. These percentages are shown in the inset of figure 10(*b*). The analogous percentages for the corresponding long-wave terms in (4.4) are shown in the inset of figure 10(*c*). We remark that the term g_1 which represents the free surface stress due to the core flow is a much larger contributor to the nonlinear balance in the long-wave model than its counterpart $\tilde{g}_1$ in the thin-film model. This suggests that, as in the case of periodic solutions to the evolution equation found in the previous section, the free surface stress due to the core flow is underestimated by the thin-film model; this agrees with the larger amplitudes that this model's travelling waves can attain, as free surface stress can act as a limiting factor to amplitude growth.

Finally, we note that by fitting the parameter $\tilde{S}$ in the thin-film model its solutions can be brought to provide better approximations to their long-wave model counterparts. Figure 11 compares the same long-wave solution for $\tilde{S} = 0.5$ as shown

in figure 10 with the thin-film model solution for $\tilde{S} = 0.2$. While still significantly
larger, the amplitude of the thin-film solution is now closer to that of the long-wave
model. Moreover, the relative contributions of the various thin-film terms shown in
figure 10(*b*) closely mirror the contributions of the long-wave terms shown in (*c*).
This suggests that an alternative definition of the function $\tilde{S}(S)$ could improve the
thin-film model's ability to represent the dynamical effects due to cylindrical geometry
for a wider range of film thicknesses.

4.3. *Streamline patterns of travelling waves and mass transport*

To examine the flow pattern of the fluid comprising the annular film in the wave
frame, it useful to look at the streamfunction defined by the annular fluid's radial and
axial velocity components u and w respectively. The streamfunction is

$$u = -\partial_z \Psi, \quad w - c = \frac{1}{r}\partial_r(r\Psi), \tag{4.8a,b}$$

$$\tilde{u} = -\partial_z \tilde{\Psi}, \quad \tilde{w} - \tilde{c} = \partial_y \tilde{\Psi} \tag{4.9a,b}$$

for the long-wave and thin-film models respectively; here, $y = (a - r)/(a - 1)$ is
a stretched radial coordinate for the thin-film models. A straightforward calculation
shows that

$$
\begin{aligned}
\Psi =&\ \left[-\frac{1}{R^4} + \frac{4S}{R^2}(R_z + R^2 R_{zzz}) \right] \left(\frac{r^3}{4} - \frac{a^2 r}{2} + \frac{a^4}{4r} \right) \\
&- 8S(R_z + R^2 R_{zzz}) \left(-\frac{r}{4} + \frac{a^2}{4r} + \frac{r}{2}\log\left(\frac{r}{a}\right) \right) - \frac{cr}{2},
\end{aligned} \tag{4.10}
$$

$$\tilde{\Psi} = -\frac{y^2}{2} + \tilde{c}y + \frac{S}{2}(h_z + h_{zzz})(y^3 - 3hy^2) \tag{4.11}$$

respectively.

Streamline patterns for three travelling wave solutions to model (LW-P) are depicted
in figure 12, where the fluid thickness parameter $a = 1.25$ for all three solutions.
For small values of S as in figure 12(*a*), the streamlines are fanned and constricted
by the interfacial disturbance; such waves will be referred to as 'shear-enhancing'
waves. For larger values of S as in figure 12(*b,c*), the additional feature of a region
of fluid recirculation, or trapped core, near the wave crest is seen by the presence of
closed streamlines; we will refer to these as 'mass-transport' waves. The volume of
the recirculation region for travelling wave solutions is shown as a function of S in
figure 12(*d*). (We note that the absence of a recirculation region in figure 12(*a*) is
not an artefact from lack of resolution, a point considered in more detail in Camassa
et al. 2012.) The wave solutions thus undergo a transition from shear-enhancing waves
to mass-transport waves as S increases. For some critical value of S, defined as the
largest value for which no recirculation region exists (in figure 12 this is $S_c \approx 0.6$),
there is exactly one stationary point (in the travelling reference frame) at the wave
crest. As S increases past S_c, this one fixed point produces three fixed points: two
hyperbolic points at the free surface, which are endpoints of a separatrix dividing the
closed streamlines from the open ones, and one elliptic fixed point at the centre of
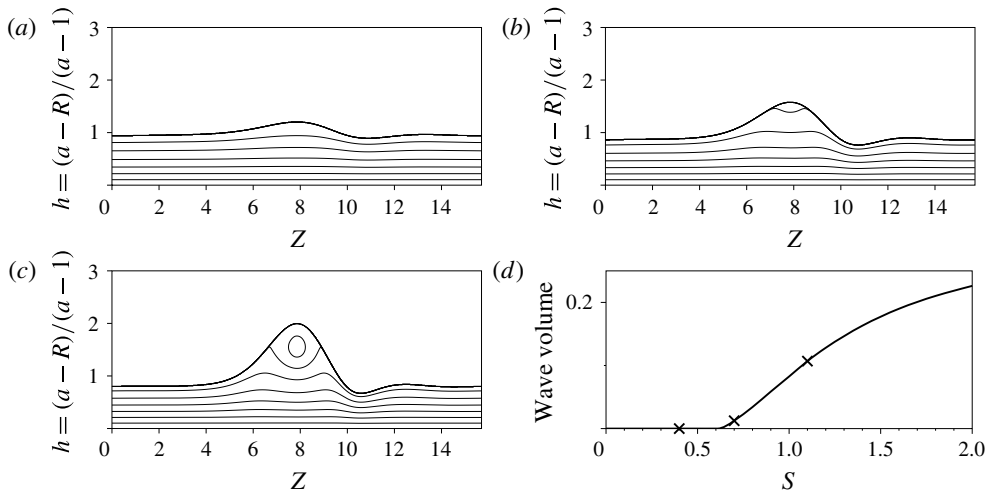the closed streamlines. This change of streamline pattern as the parameters vary can

FIGURE 12. (*a*–*c*) Streamlines plotted in a travelling reference frame for solutions to the long-wave model (LW-P) for varying values of S (0.4 (*a*), 0.7 (*b*), 1.1 (*c*)) and $a = 1.25$. (*d*) Volume of the recirculation region as a function of S. For $a = 1.25$, $S < 0.6$, no recirculation region exists. Each cross corresponds to one of the three solutions shown.

be viewed as a bifurcation of the characteristic equations (4.8) and (4.9) governing the fluid parcel motion.

Streamline patterns for $S = 1$ and varying film thickness parameter a are shown in figure 13(*a*–*e*). As the film thins, the waves again transition from shear-enhancing waves to mass-transport waves. Figure 13(*f*) shows the dependence of the wave volume on the film thickness. It is interesting to note that there is some film thickness for which the wave volume is maximized (in figure 13 this is $a \approx 1.1$). The volume of a recirculation region in films thinner than this critical thickness is limited by the amount of liquid in the domain. For thicker films, wave amplitudes are suppressed by the core flow, as discussed in §4.1; increasing film thickness thus restricts, and eventually eliminates altogether, the size of the recirculation region.

Figure 14 shows the streamlines for various values of the surface tension parameter $\tilde{S}$ for the thin-film model (TF-P). Unlike solutions to (LW-P), there is no transition from shear-enhancing waves to mass-transport waves; all waves are found to be mass-transport waves. Three fixed points exist in all wave solutions: two on the free surface and one in the recirculation zone, as described above. The volume of the recirculation region vanishes as $\tilde{S} \to 0$. This difference in streamline topology is summarized in figure 15, where the regions of mass-transport versus shear-enhancing waves for (LW-P) are shown in S–a parameter space. The vertical boundary on the left represents the thin-film limit $a \to 1$.

The degree to which the recirculation region contributes to the overall annular flux in travelling wave solutions to (LW-P) can be quantified by separating the total annular flux into the portion due to the recirculation region and the portion due to the underlying substrate, i.e.

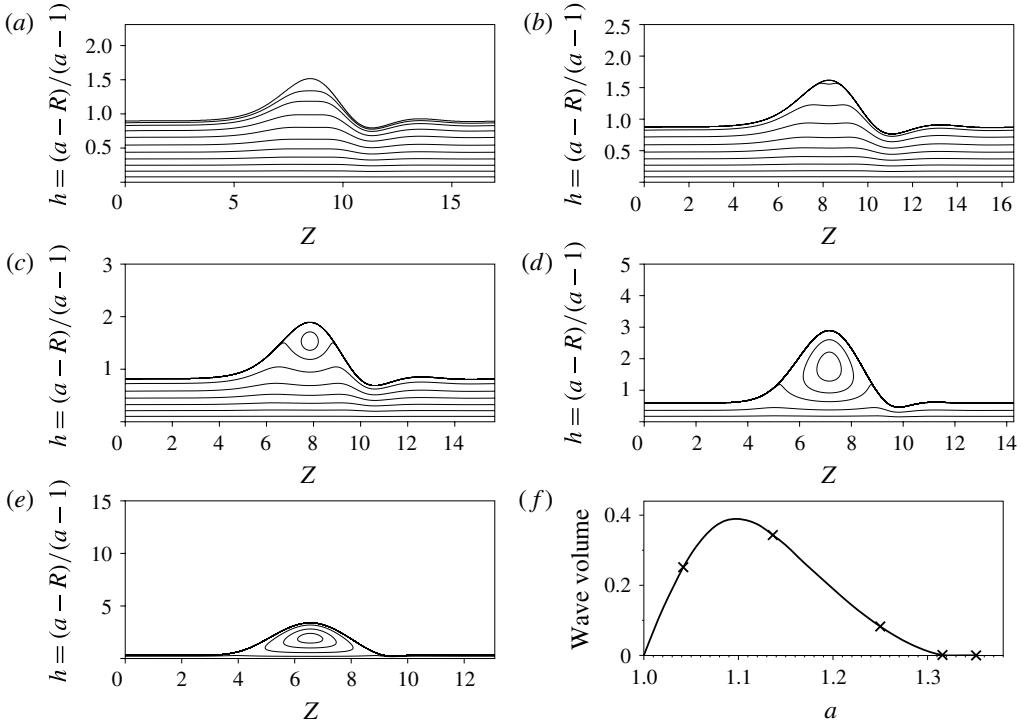$$q_r^{(a)}(Z, t) = 2\pi \int_R^{R^*} wr \, \mathrm{d}r, \quad q_s^{(a)}(Z, t) = 2\pi \int_{R^*}^{a} wr \, \mathrm{d}r \qquad (4.12a,b)$$

FIGURE 13. (a–e) The same as figure $12(a$–$c)$ but for fixed $S = 1$ and varying a (1.35 (a), 1.32 (b), 1.25 (c), 1.14 (d), 1.04 (e)). (f) The volume of the recirculation region as a function of a. For thick films ($a > 1.32$ when $S = 1$) no recirculation region exists.
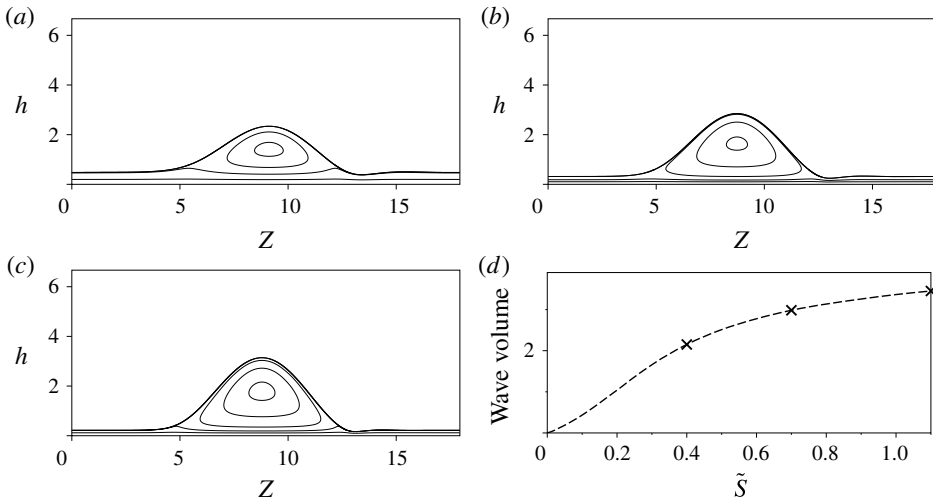

FIGURE 14. (a–c) The same as figure $12(a$–$c)$ but for (TF-P) ($S = 0.4$ (a), 0.7 (b), 1.1 (c)). (d) The volume of the recirculation region as a function of $\tilde{S}$; every travelling wave has a non-zero volume of fluid inside a recirculation region.
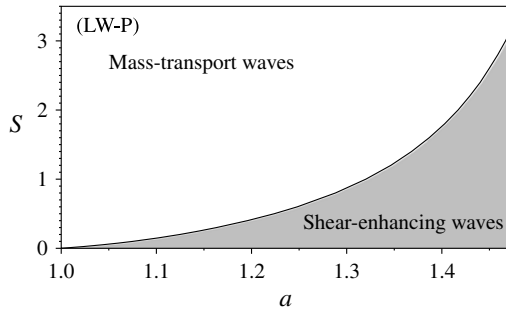
FIGURE 15. Regions of *S*–*a* parameter space where mass-transport waves or shear-enhancing waves exist for the long-wave model (LW-P).
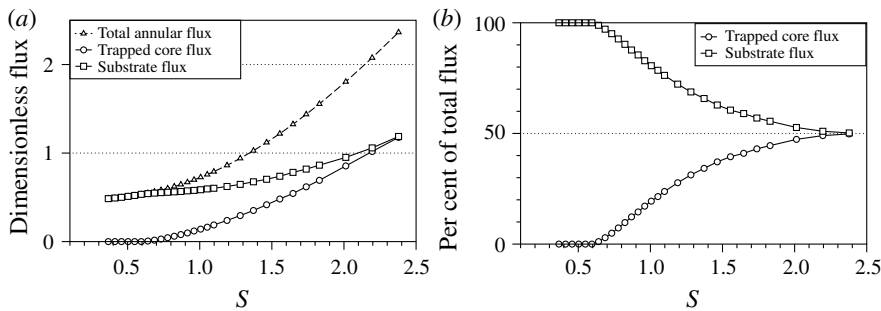

FIGURE 16. (*a*) The total dimensionless flux $m\langle q^{(a)}\rangle$ for travelling wave solutions to (LW-P) with $a = 1.25$. The volume fluxes due to the recirculation region $m\langle q_r^{(a)}\rangle$ and the substrate $m\langle q_s^{(a)}\rangle$ are shown as well. (*b*) Percentage of the total flux due to the recirculation region and substrate in (*a*).

respectively, where $R^*(Z)$ denotes the radial location of the separatrix at locations Z that lie within the domain of the recirculation region, and $R^*(Z) = R(Z)$ for all other Z. Each quantity in (4.12) can be averaged over one wavelength, i.e. $\langle q_r^{(a)}\rangle$ and $\langle q_s^{(a)}\rangle$, where $\langle \cdot \rangle = L^{-1} \int_0^L \cdot \, \mathrm{d}Z$. Figure 16(*a*) shows each of these quantities, as well as the average total flux $\langle q^{(a)}\rangle$, for solutions with $a = 1.25$ and varying S; it should be noted that in (*a*) the dimensionless annular volume flux has been rescaled by the viscosity ratio $m = \mu^{(a)}/\mu^{(c)}$ as liquid scales are being emphasized here. The percentage that each portion of the flux contributes is shown in figure 16(*b*). Consistent with figure 12, no recirculation region exists for $S \leqslant S_c \approx 0.6$. For larger S values, as S increases, the recirculation region grows in size and contributes an increasingly large fraction of the total flux. We note that the percentage of flux attributable to the recirculation region appears to converge to 50 % in the limit of large S in (*b*), though this limiting value cannot be expected to hold for all values of the film thickness parameter a.

The source of the difference in behaviour between the two models is worth discussing. We remark that a recirculation region can only exist when the speed of a fluid parcel somewhere on the free surface is identical to the wave speed; such a parcel would be located at one of the two fixed stagnation points lying on the free surface in the travelling reference frame. The velocity of a fluid parcel lying on an

unperturbed interface in the long-wave (LW-P) and thin-film (TF-P) models is

$$w = a^2 - 1 = 2\beta + \beta^2, \left.\vphantom{\begin{matrix}a\\b\end{matrix}}\right\}$$
$$\tilde{w} = 2(a - 1) = 2\beta \qquad (4.13)$$

respectively. The phase speed of a linear disturbance is the real part of ω/k in (3.2) and (3.3),

$$c = a^4 - a^2 = 2\beta + 5\beta^2 + O(\beta^3), \left.\vphantom{\begin{matrix}a\\b\end{matrix}}\right\}$$
$$\tilde{c} = 2(a - 1) = 2\beta. \qquad (4.14)$$

Thus, in model (TF-P) the fluid can match the wave speed, $\tilde{w} = \tilde{c}$, and it can be expected that there exist fluid parcels moving at the speed of the wave regardless of how small the free surface disturbance is. The long-wave model (LW-P), however, has a larger disturbance speed than interface speed, i.e. $w < c$, guaranteeing that no recirculation region can exist for small-amplitude waves.

We stress that simply retaining one additional power of β in the hyperbolic terms is sufficient to prevent this phenomenon of persistence of closed streamlines at all travelling wave amplitudes from occurring in the thin-film model. If $F = 0$ in (TF-PG), then the phase speed of a linear disturbance in (TF-PG) is now given by $\tilde{c}_2 = 2\beta + 5\beta^2 = c + O(\beta^3)$, while the speed of the undisturbed interface is $\tilde{w}_2 = w$; thus the higher-order thin-film model (TF-PG) contains the same streamline bifurcation as seen in its long-wave counterpart.

5. Discussion

The analytical and numerical results in §§ 3 and 4 have demonstrated a variety of qualitative differences in model behaviour that can arise when the thin-film approximation is applied to a long-wave model. We next show how the models (TF-P), (TF-PG), (LW-P) and (LW-PG) fit into an extended hierarchy of asymptotic models, and discuss whether the qualitative differences presented in the previous sections are seen in these models.

The primary long-wave model (LW-PG) was derived by assuming an asymptotic balance of three terms representing stress due to the core flow, gravity and capillary forces, and in the case of small density difference between the fluids, i.e. $l \ll 1$, the model reduced to (LW-P). In the case of weak core flow, i.e. $C \ll 1$ and $lRe/Fr^2 \gg 1$, the primary model reduces to the model equation derived by Camassa *et al.* (2014) (after a rescaling in time by F rather than $1/m$),

$$R_t - f_2(R; a)R_z + \frac{S'(a)}{R}[f_3(R; a)(R_z + R^2 R_{zzz})]_z = 0, \qquad (5.1)$$

where $S' \equiv S/F$. Equation (5.1) is similar to that derived in Lin & Liu (1975) for interior and exterior flows, and is analogous to the exterior models derived in Craster & Matar (2006) and Kliakhandler, Davis & Bankoff (2001).

In the case of both weak core flow and near-equal density fluids, i.e. $C \ll 1$ and $C \ll lRe/Fr^2$, capillary forces dominate the dynamics, and the primary model reduces to (after a rescaling in time by $1/C$ rather than $1/m$)

$$R_t + \frac{1}{R}[f_3(R; a)(R_z + R^2 R_{zzz})]_z = 0. \qquad (5.2)$$

Model	$\bar{Q}^{(c)}$	l	Number of model parameters	Reference
(2.17)–(LW-PG)	>0	$\neq0$	3	Camassa *et al.* (2012)
(2.20)–(LW-P)	>0	$=0$	2	Camassa & Lee (2006)
(5.1)–(LW-G)	$=0$	$\neq0$	2	Camassa *et al.* (2014); exterior flows: Craster & Matar (2006)
(5.2)–(LW)	$=0$	$=0$	1	

TABLE 1. Summary of long-wave models.

Model	$\bar{Q}^{(c)}$	l	Number of model parameters	Reference
(2.23)–(TF-PG)	>0	$\neq0$	2	
(2.24)–(TF-P)	>0	$=0$	1	Kerchman (1995)
(5.3)–(TF-G)	$=0$	$\neq0$	1	Frenkel (1992)
(5.4)–(TF)	$=0$	$=0$	0	Hammond (1983)

TABLE 2. Summary of thin-film models.

For ease of reference we label models (5.1) and (5.2) with the tags (LW-G) and (LW). It should be noted that the time scale for each of the four long-wave models (LW-PG), (LW-P), (LW-G) and (LW) is different, with each rescaling of time corresponding to a reduction of the number of model parameters by one. Table 1 summarizes the four long-wave models; the values of the core volume flow rate $\bar{Q}^{(c)}$ and the difference in density between the two fluids l appropriate to each model are given, as is a reference where the model derivation can be found in the literature.

Likewise, similar reductions can be made to the primary thin-film model (TF-PG). In the case of weak core flow, retaining $O(\beta^2)$ hyperbolic terms only and employing a rescaling in time analogous to that used in deriving the long-wave gravity-driven model (LW-G)/(5.1) produces

$$h_t - h^2 h_z + \tilde{S}'[h^3(h_z + h_{zzz})]_z = 0, \qquad (5.3)$$

where $\tilde{S}' = 8\beta S'/3$. Equation (5.3) is the thin-film counterpart to the gravity-driven long-wave model (LW-G) and was derived by Frenkel (1992) using slightly different scalings; it was subsequently studied analytically and numerically by Kalliadasis & Chang (1994) and Kerchman & Frenkel (1994), among others.

Similarly, in the case of both weak core flow and nearly equal density fluids, (2.23) simplifies to the evolution equation studied by Hammond (1983) after a rescaling of time by $t' = (16\beta^3 S/3)t$, immediately dropping primes again,

$$h_t + [h^3(h_z + h_{zzz})]_z = 0. \qquad (5.4)$$

A summary of the four thin-film models is given in table 2.

The long-wave models and their thin-film counterparts form a natural hierarchy illustrated in figure 17. The number of parameters that govern the dynamics of each model is indicated by the axis on the left.

A few comments are now in order. First, we note that the thin-film models (TF-G) and (TF) apply to both interior and exterior liquid coatings; the hierarchy in figure 17
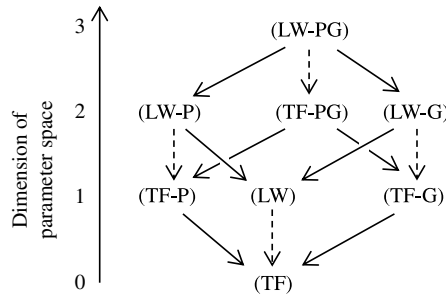
FIGURE 17. The primary long-wave model (2.17)–(LW-PG) reduces to (2.20)–(LW-P) in the absence of gravity or to (5.1)–(LW-G) in the absence of pressure-driven core flow; the elimination of both forces results in (5.2)–(LW). Each long-wave model also corresponds to a thin-film model to which it reduces in the thin-film limit. The number of parameters governing the dynamics of each model is also shown.

thus overlaps with that outlined in Craster & Matar (2009), with (LW-G) being the analogue to the exterior long-wave model in Craster & Matar (2006).

Second, the thin-film models are all conservation laws. However, the conserved quantity in these thin-film models is not the film's mass but the film's thickness h; mass is therefore only conserved in an approximate flattened-geometry sense. In contrast, the long-wave models conserve the quantity R^2, thus representing the mass in the full cylindrical geometry. In fact, the (trivial) flat solution $R = 1$ of the long-wave models can recover its exact counterpart (2.9)–(2.10) for the full governing equation, while the analogous solution for the thin-film models can only lead to an approximation, as these models are limited by the geometric rectification of an annular cross section valid only in the limit of small film thickness.

Next, we note that keeping higher-order terms in β would in principle allow for thin-film models that potentially capture more physical effects. For example, in the case of gravity-driven flow, i.e. let $F = 0$ in the primary thin-film model (TF-PG), retaining an extra order in β for all terms (including the capillary terms) produces a model analogous to that derived for gravity-driven exterior liquid coatings by Roy, Roberts & Simpson (2002). Their model conserves mass and includes some effects of the cylindrical geometry not contained in (TF-G). (The model derived in Roy *et al.* 2002 can be accurately said to be a 'thin-film' model, but has much in common with its long-wave counterpart derived in Kliakhandler *et al.* 2001 and Craster & Matar 2006.)

Finally, we note that some, but not all, of the qualitative differences seen between the long-wave and thin-film models for core–annular flow are also seen in gravity-driven models. For instance, in the case of exterior flows, Roy *et al.* (2002) note that (TF-G) produces higher-amplitude waves with slower speed than those obtained by models that retain the curved geometry, consistent with the core–annular results shown in figure 6. However, in interior gravity-driven flow the streamline bifurcation discussed in § 4.3 occurs in both the long-wave (LW-G) and thin-film (TF-G) models; the speed of a fluid parcel at the free surface is half the speed of an infinitesimal free surface disturbance, guaranteeing that a recirculation region cannot exist in a small-amplitude wave. Only for sufficiently large $\tilde{S}'$ does the nonlinear balance of terms create a large enough wave amplitude and free surface speed to allow for a recirculation region to form; numerically it was found that $\tilde{S}' > 1$ was
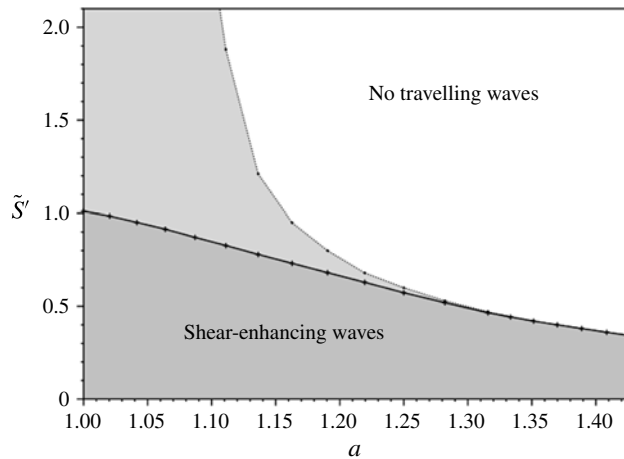
FIGURE 18. Regions of $\tilde{S}'$–a parameter space where mass-transport waves and/or shear-enhancing waves were found numerically for model (LW-G).

sufficient to allow the formation of a recirculation region in (TF-G). Thus, truncation to the leading-order hyperbolic term in β does not result in the same streamline topology change as seen in the pressure-driven flow. Figure 18 shows the region of $\tilde{S}'$–a parameter space in which shear-enhancing travelling wave solutions to (LW-G) were found; see Camassa *et al.* (2014) for further discussion.

6. Conclusions

We have studied a collection of long-wave and thin-film models for the problem of pressure-driven viscous core–annular flow, and examined their dynamical differences with respect to the asymptotic assumptions made in the process of model derivation. While the thin-film model equations have simpler nonlinearities and a parameter space that is one dimension smaller than their long-wave counterparts, these simplifications come at the expense of neglecting aspects of the cylindrical geometry of the problem.

In particular, we have shown how this cylindrical geometry makes an important contribution to the behaviour of the film flow, since sufficiently large-amplitude waves 'feel' the presence of the tube centre through self-interaction across the wave crest and/or the constricted core fluid dynamics. Significant differences exist in the qualitative behaviour of both the evolution of the free surface and the underlying fluid flow between each class of model. It was seen that, given a set of parameter values, the long-time behaviour of the free surface, the nature of the free surface instabilities and the topology of streamlines in a travelling reference frame all depend on the class of the model. Thin-film models such as (TF-PG), which retain higher-order terms (analogous to the model derived by Roy *et al.* (2002) for the case of a gravity-driven exterior liquid coating), can eliminate, at least on a qualitative level, these differences with respect to their long-wave counterparts. These extra terms, of course, compromise the simplicity offered by the leading-order thin-film models. Since long-wave models used in the literature for both interior and exterior liquid coatings, e.g. Craster & Matar (2006) and Camassa *et al.* (2014), have been shown to give good agreement with experiments in Smolka, North and Guerra (2008) and Camassa *et al.* (2014) respectively, one of the conclusions of our study is that it seems advisable to use the full cylindrical geometry offered by long-wave modelling whenever possible.

Appendix A. Long-wave expansion for fully coupled core–annular flow

A systematic expansion of the dimensionless governing equations in ϵ results in a leading-order long-wave solution

$$w_{LW}^{(a)} = \frac{1}{4m} \left[\left(p_z^{(a)} + \frac{(l+1)Re}{Fr^2} \right) (r^2 - a^2) - \frac{2l\,Re}{Fr^2} R^2 \log \frac{r}{a} \right], \tag{A 1}$$

$$w_{LW}^{(c)} = \frac{1}{4} \left(p_z^{(c)} + \frac{Re}{Fr^2} \right) (r^2 - R^2)$$
$$+ \frac{1}{4m} \left[\left(p_z^{(a)} + \frac{(l+1)Re}{Fr^2} \right) (R^2 - a^2) - \frac{2l\,Re}{Fr^2} R^2 \log \frac{1}{a} \right], \tag{A 2}$$

where we have also assumed $\epsilon Re \ll 1$, allowing the inertial terms to be neglected. This solution is a dimensionless slowly varying z-dependent modulation of (2.9)–(2.10). Integrating each of the velocity profiles (A 1)–(A 2) across their respective domains as in (2.14a,b) results in the following expressions for the dimensionless volume flux:

$$q^{(a)} = \frac{\pi R^4}{8m} \left[-\left(1 - \frac{a^2}{R^2} \right)^2 \left(p_z^{(a)} + \frac{(l+1)Re}{Fr^2} \right) - \frac{2l\,Re}{Fr^2} \left(1 - \frac{a^2}{R^2} - 2\log \frac{R}{a} \right) \right], \tag{A 3}$$

$$q^{(c)} = \frac{\pi}{8} \left[-\left(p_z^{(c)} + \frac{Re}{Fr^2} \right) + \frac{2}{m} \left(1 - \frac{a^2}{R^2} \right) \left(p_z^{(a)} + \frac{(l+1)Re}{Fr^2} \right) - \frac{4l\,Re}{m\,Fr^2} \log \frac{R}{a} \right], \tag{A 4}$$

where the z dependence enters the right-hand sides through the slowly varying functions $p^i(z, t)$ and $R(z, t)$.

Extraction of the dimensionless pressure gradient from the total flux invariance (2.15) yields the leading-order expression

$$p_z^{(a)} = \left[\frac{1}{C} \left(\frac{R_z}{R^2} + R_{zzz} \right) - \frac{Re}{Fr^2} - \frac{\pi}{2R^4} \left(1 + Q^{(a)} \right) - \frac{Re(l+1)}{2m\,Fr^2} \left(1 - \frac{a^2}{R^2} \right)^2 \right.$$
$$\left. + \frac{Re}{m\,Fr^2} \left(1 - \frac{a^2}{R^2} \right) \right] \Big/ \left[1 - \frac{1}{m} \left(1 - \frac{a^4}{R^4} \right) \right], \tag{A 5}$$

where $Q^{(a)} = \bar{Q}^{(a)}/\bar{Q}^{(c)}$ is the dimensionless annular flux. This expression can be simplified by assuming a balance between its first three terms, i.e.

$$C = O(1), \quad Fr^2 = O(Re), \tag{A 6a,b}$$

and by also assuming that both

$$m \gg (a/\tilde{R})^4, \quad m \gg l(a/\tilde{R})^4 \tag{A 7a,b}$$

hold true, where $\tilde{R}$ is a characteristic value for the core radius such that $R(z, t) = O(\tilde{R})$ for all z and t. It should be noted that the asymptotic ordering (A 7) implies that the fluxes in (A 3)–(A 4) satisfy $q^{(a)} \ll 1$ and $q^{(c)} = O(1)$. Given both (A 6) and (A 7), the pressure gradient (A 5) can be approximated by

$$p_z^{(a)} = \frac{1}{C}\left(\frac{R_z}{R^2} + R_{zzz}\right) - \frac{Re}{Fr^2} - \frac{\pi}{2R^4}; \tag{A 8}$$

substitution of (A 8) into (A 3) and (2.16) results in the primary long-wave model (2.17). We remark that the ordering (A 7) will not hold if the core region becomes excessively narrow. In this case, the problem can be termed a 'thick-film' problem; see, e.g., Lowman & Hoeffer (2013) for a model of a similar problem.

The dimensional forms of (A 1)–(A 5) and (A 8) are given for reference. The dimensional velocities are

$$\bar{w}_{LW}^{(a)} = \frac{\bar{r}^2 - \bar{a}^2}{4\mu^{(a)}}(\bar{p}_{\bar{z}}^{(a)} + \rho^{(a)}g) + \frac{g\bar{R}^2}{2\mu^{(a)}}(\rho^{(c)} - \rho^{(a)})\log\left(\frac{\bar{r}}{\bar{a}}\right), \tag{A 9}$$

$$\bar{w}_{LW}^{(c)} = \frac{\bar{r}^2 - \bar{R}^2}{4\mu^{(c)}}(\bar{p}_{\bar{z}}^{(c)} + \rho^{(c)}g)$$
$$+ \frac{\bar{R}^2 - \bar{a}^2}{4\mu^{(a)}}(\bar{p}_{\bar{z}}^{(a)} + \rho^{(a)}g) + \frac{g\bar{R}^2}{2\mu^{(a)}}(\rho^{(c)} - \rho^{(a)})\log\left(\frac{\bar{R}}{\bar{a}}\right), \tag{A 10}$$

the dimensional fluxes are

$$\bar{q}^{(a)} = \frac{\pi\bar{R}^4}{8\mu^{(a)}}\left[-\left(1 - \frac{\bar{a}^2}{\bar{R}^2}\right)^2 (\bar{p}_{\bar{z}}^{(a)} + \rho^{(a)}g) + 2g(\rho^{(c)} - \rho^{(a)})\left(1 - \frac{\bar{a}^2}{\bar{R}^2} - 2\log\frac{\bar{R}}{\bar{a}}\right)\right], \tag{A 11}$$

$$\bar{q}^{(c)} = \frac{\pi\bar{R}^4}{8\mu^{(a)}}\left[-\frac{\mu^{(a)}}{\mu^{(c)}}(\bar{p}_{\bar{z}}^{(c)} + \rho^{(c)}g) + 2\left(1 - \frac{\bar{a}^2}{\bar{R}^2}\right)(\bar{p}_{\bar{z}}^{(a)} + \rho^{(a)}g) + 4g(\rho^{(c)} - \rho^{(a)})\log\frac{\bar{R}}{\bar{a}}\right], \tag{A 12}$$

the dimensional pressure gradient is

$$\bar{p}_{\bar{z}}^{(a)} = \left[\frac{\gamma}{\bar{R}^2}(\bar{R}_{\bar{z}} + \bar{R}^2\bar{R}_{\bar{z}\bar{z}\bar{z}}) - \rho^{(c)}g - \frac{8\bar{Q}\mu^{(c)}}{\pi\bar{R}^4} + \frac{\mu^{(c)}}{\mu^{(a)}}\left[2g\rho^{(c)}\left(1 - \frac{\bar{a}^2}{\bar{R}^2}\right)\right.\right.$$
$$\left.\left. - g\rho^{(a)}\left(1 - \frac{2\bar{a}^2}{\bar{R}^2} + \frac{\bar{a}^4}{\bar{R}^4}\right)\right]\right] \Big/ \left[1 - \frac{\mu^{(c)}}{\mu^{(a)}}\left(1 - \frac{\bar{a}^4}{\bar{R}^4}\right)\right] \tag{A 13}$$

and the approximate dimensional pressure gradient used to derive (2.17) is

$$\bar{p}_{\bar{z}}^{(a)} \approx \frac{\gamma}{\bar{R}^2}(\bar{R}_{\bar{z}} + \bar{R}^2\bar{R}_{\bar{z}\bar{z}\bar{z}}) - \rho^{(c)}g - \frac{8\bar{Q}^{(c)}\mu^{(c)}}{\pi\bar{R}^4}. \tag{A 14}$$

REFERENCES

BERS, A. 1983 Space–time evolution of plasma instabilities – absolute and convective. In *Handbook of Plasma Physics* (ed. M. N. Rosenbluth & R. Z. Sagdeev), vol. I, pp. 451–517. North-Holland.

BRIGGS, R. J. 1964 *Electron-Stream Interaction with Plasmas*. MIT Press.

CAMASSA, R., FOREST, M. G., LEE, L., OGROSKY, H. R. & OLANDER, J. 2012 Ring waves as a mass transport mechanism in air-driven core–annular flows. *Phys. Rev.* E **86**, 066305,1–11.

CAMASSA, R. & LEE, L. 2006 *Advances in Engineering Mechanics – Reflections and Outlooks* (ed. A. Chwang, M. Teng & D. Valentine), pp. 222–238. World Scientific.

CAMASSA, R., OGROSKY, H. R. & OLANDER, J. 2014 Viscous film flow coating the interior of a vertical tube. Part I. Gravity-driven flow. *J. Fluid Mech.* **745**, 682–715.

CAMPANA, D. M., UBAL, S., GIAVEDONI, M. & SAITA, F. 2007 Stability of the steady motion of a liquid plug in a capillary tube. *Ind. Engng Chem. Res.* **46**, 1803–1809.

CHANG, H.-C., DEMEKHIN, E. A. & KOPELEVICH, D. I. 1993 Laminarizing effects of dispersion in an active-dissipative nonlinear medium. *Physica* D **63**, 299–320.

CRASTER, R. V. & MATAR, O. K. 2006 On viscous beads flowing down a vertical fibre. *J. Fluid Mech.* **553**, 85–105.

CRASTER, R. V. & MATAR, O. K. 2009 Dynamics and stability of thin liquid films. *Rev. Mod. Phys.* **81**, 1131–1198.

DUPRAT, C., RUYER-QUIL, C., KALLIADASIS, S. & GIORGIUTTI-DAUPHINE, F. 2007 Absolute and convective instabilities of a viscous film flowing down a vertical fiber. *Phys. Rev. Lett.* **98**, 244502.

FRENKEL, A. L. 1992 Nonlinear theory of strongly undulating thin films flowing down vertical cylinders. *Europhys. Lett.* **18**, 583–588.

GOREN, S. L. 1962 The instability of an annular thread of fluid. *J. Fluid Mech.* **27**, 309–319.

HAMMOND, P. S. 1983 Nonlinear adjustment of a thin annular film of viscous fluid surrounding a thread of another within a circular cylindrical pipe. *J. Fluid Mech.* **137**, 363–384.

HICKOX, C. 1971 Instability due to viscosity and density stratification in axisymmetric pipe flow. *Phys. Fluids* **14**, 251–262.

HUERRE, P. & MONKEWITZ, P. A. 1990 Local and global instabilities in spatially developing flows. *Annu. Rev. Fluid Mech.* **22**, 473–537.

JOHNSON, M. A. *et al.* 2015 Spectral stability of periodic wave trains of the Korteweg–de Vries/Kuramoto–Sivashinsky equation in the Korteweg–de Vries limit. *Trans. Amer. Math. Soc.* **367**, 2159–2212.

JOSEPH, D. D. & RENARDY, Y. 1993 *Fundamentals of Two-Fluid Dynamics, Part 2: Lubricated Transport, Drops, and Miscible Liquids*. Springer.

KALLIADASIS, S. & CHANG, H.-C. 1994 Drop formation during coating of vertical fibers. *J. Fluid Mech.* **261**, 135–168.

KERCHMAN, V. I. 1995 Strongly nonlinear interfacial dynamics in core–annular flows. *J. Fluid Mech.* **290**, 131–166.

KERCHMAN, V. I. & FRENKEL, A. L. 1994 Interactions of coherent structures in a film flow: simulations of a highly nonlinear evolution equation. *Theor. Comput. Fluid Dyn.* **6**, 235–254.

KLIAKHANDLER, I. L., DAVIS, S. H. & BANKOFF, S. G. 2001 Viscous beads on vertical fibre. *J. Fluid Mech.* **429**, 381–390.

KURAMOTO, Y. & TSUZUKI, T. 1976 Persistent propagation of concentration waves in dissipative media far from thermal equilibrium. *Progr. Theoret. Phys.* **55**, 356–369.

LIN, S. P. & LIU, W. C. 1975 Instability of film coating of wires and tubes. *AIChE J.* **24**, 775–782.

LOWMAN, N. K. & HOEFFER, M. A. 2013 Dispersive hydrodynamics in viscous fluid conduits. *Phys. Rev.* E **88**, 023016.

OGAWA, T. 1994 Traveling wave solutions to a perturbed Korteweg–de Vries equation. *Hiroshima Math J.* **24**, 401–422.

OGROSKY, H. R. 2013 Modeling liquid film flow inside a vertical tube. Diss. University of North Carolina.

ORON, A., DAVIS, S. H. & BANKOFF, S. G. 1997 Long-scale evolution of thin liquid films. *Rev. Mod. Phys.* **69**, 932–980.

PAPAGEORGIOU, D. T., MALDARELLI, C. & RUMSCHITZKI, D. S. 1990 Nonlinear interfacial stability of core–annular film flows. *Phys. Fluids* A **2** (3), 340–352.

ROY, R. V., ROBERTS, A. J. & SIMPSON, M. E. 2002 A lubrication model of coating flows over a curved substrate in space. *J. Fluid Mech.* **454**, 235–261.

SIVASHINSKY, G. I. & MICHELSON, D. M. 1980 On irregular wavy flow of a liquid film down a vertical plane. *Progr. Theoret. Phys.* **63**, 2112–2114.

SMOLKA, L., NORTH, J. & GUERRA, B. 2008 Dynamics of free surface perturbations along an annular viscous film. *Phys. Rev.* E **77**, 036301.

UBAL, S. *et al.* 2008 Stability of the steady-state displacement of a liquid plug driven by a constant pressure difference along a prewetted capillary tube. *Ind. Engng Chem. Res.* **47**, 6307–6315.

VELLINGIRI, R., TSELUIKO, D. & KALLIADASIS, S. 2015 Absolute and convective instabilities in counter-current gas–liquid film flows. *J. Fluid Mech.* **763**, 166–201.

YIH, C.-S. 1967 Instability due to viscosity stratification. *J. Fluid Mech.* **27**, 337–352.